Thermal-Driven Graupel Generation Process to Explain Dry-Season Convective Vigor over the Amazon

Authors: Toshi Matsui[1&2], Daniel Hernandez-Deckers[3], Scott E. Giangrande[4], Thiago S. Biscaro[5], Ann Fridlind[6], and Scott Braun[1]

[1] *Mesoscale Atmospheric Processes Laboratory, NASA Goddard Space Flight Center, Greenbelt, MD, USA*

[2] *Earth System Science Interdisciplinary Center – ESSIC, University of Maryland, College Park, MD, USA*

[3] *Grupo de Investigación en Ciencias Atmosféricas, Departamento de Geociencias, Universidad Nacional de Colombia, Bogotá, Colombia*

[4] *Environmental and Climate Sciences Department, Brookhaven National Laboratory, Upton, NY, USA*

[5] *Meteorological Satellites and Sensors Division, National Institute for Space Research, Cachoeira Paulista, São Paulo, Brazil*

[6] *NASA Goddard Institute for Space Studies, New York, NY, USA*

Submitted to EGU Atmospheric Chemistry and Physics (ACP)

Correspondence to: Toshi Matsui, Toshihisa.Matsui-1@nasa.gov

Formatted: Font: (Default) Times New Roman

Abstract. Large-eddy simulations (LESs) are conducted for each day of the intensive observation periods (IOPs) of the Green Ocean Amazon (GoAmazon) field campaign to characterize the updrafts and microphysics within deep convective cores while contrasting those properties between Amazon wet and dry seasons. Mean Doppler velocity (V_{dop}) simulated using LESs are compared with 2-year measurements from a Radar Wind Profiler (RWP) as viewed by statistical composites separated according to wet and dry season conditions. In the observed RWP and simulated LES V_{dop} composites, we find more intense low-level updraft velocity, vigorous graupel generation, and intense surface rain during the dry periods than the wet periods. To investigate coupled updraft-microphysical processes further, single-day golden cases are selected from the wet and dry periods to conduct detailed cumulus thermal tracking analysis. Tracking analysis reveals that simulated dry-season environments generate more droplet-loaded low-level thermals than wet-season environments. This tendency correlates with seasonal contrasts in buoyancy and vertical moisture advection profiles in large-scale forcing. Employing a normalized time series of mean thermal microphysics, the simulated cumulus thermals appear to be the primary generator of cloud droplets. When subsequent thermals penetrate the ice crystal layer, droplets within the thermals interact with entrained ice crystals, which enhances riming in the thermals. This appears to be a production pathway of graupel/hail particles within simulated deep convective cores. In addition, less-diluted dry-case thermals tend to be elevated higher, and graupel grows further during sedimentation after spilling out from thermals. Therefore, greater concentrations of low-level moist thermals likely result in more graupel/hail production and associated dry-season convective vigor.

1. Introduction

Deep convection is a fundamental process of turbulence that drives the Earth's general circulation and regulates thermodynamic fields (Emanuel et al., 1994). Deep convection undergoes complex dynamical and microphysical processes throughout its life cycle, which appear as towering clouds visible from satellites in different parts of the world (Stephens et al., 2002). As a result, deep convection generates significant amounts of atmospheric latent heat, surface precipitation, and hydrometeors that reflect/absorb solar and infrared radiation, modifying atmospheric circulation and surface energy and mass fluxes (Hartmann, 2016). These complexities in deep convection and feedback processes pose significant challenges in predicting weather and climate using numerical Earth system modeling across different scales (Grabowski and Petch, 2009; Sullivan and Voigt, 2021).

Characteristics of deep convection are unique in different seasons and geographic regimes affected by the local environment. One of the most straightforward yet most robust regime separation concepts is the land-ocean (L-O) contrast (Williams and Stanfill 2002). Solar radiation increases the surface skin temperature over land more readily than over the ocean due to the smaller heat capacity of soils and vegetation than deep water bodies, thus producing stronger surface infrared flux and turbulent heat flux (Matsui and Mocko 2014). This greater surface energy deepens planetary boundary layers that may trigger deeper convective clouds depending on the atmospheric profiles (Pielke 2001). Overall, the continental environment tends to promote deeper convection with stronger, wider convective cores (Lucas et al. 1994, Wang et al. 2019), with suppressed warm rain and enhanced cold precipitation process (Williams et al. 2005), which often leads to unique drop-size distribution characteristics and precipitation partitioning between convective and stratiform process outcomes in different geographic regions (e.g., Tokay and Short 1996; Giangrande et al. 2012; Dolan et al. 2018).

Satellite observations similarly depict continental convective invigoration as characterized by more frequent lightning flashes and heavily rimed particles aloft over land than ocean (Williams et al. 2004, Zipser et al. 2006, Stolz et al. 2015, Matsui et al. 2016). Takahashi et al. (2017 & 2021)

81 show that continental convection generally contains less diluted cores than their oceanic

82 counterparts, following an inverse relationship between convective core width and dilution rate.

83 Similarly, Jeyaratnam et al. (2020) recently suggested that convective updraft and mass flux

84 properties were distinctly different between tropical land and tropical oceanic convection using

85 methods to estimate those properties that blend satellite observations with plume models. Hereafter,

86 we define "convective vigor" by the enhanced cold-precipitation process characterized by larger

87 rimed particles (graupel/hail) and large and copious raindrops in convective cores.   **Deleted:** vigorous

88

89 Representation of deep convective cloud land-ocean contrasts is still an ongoing challenge for

90 global atmospheric models at storm-resolving resolution (a few km of horizontal grid spacing),

91 partially owing to the poor representation of cloud dynamics (Matsui et al. 2016). Robinson et al.

92 (2011) configured idealized simulation setups to investigate the "island" effect of convection with

93 finer grid spacing (500 m or 1 km) and successfully simulated convective vigor equivalent to the

94 observed microwave brightness temperature. Matsui et al. (2020) used a nested regional model

95 with 1 km grid spacing to compare mid-latitude continental versus tropical maritime storms and

96 successfully reproduced land-ocean contrasts of hydrometeor identification profiles from

97 polarimetric radars.

98

99 However, statistical evaluation of simulated vertical velocity and association with convective

100 vigor process (i.e., graupel/hail generation) have not yet been examined very well due to a lack of

101 observations and detailed process-oriented model investigation, respectively. For example,

102 mesoscale convective system (MCS) studies performed by Prein et al. (2022) and Ramos-Valle et

103 al. (2023) highlight the challenges when attempting to represent continental convection within the

104 constraints of limited observations while attempting to establish optimal configurations as a

105 function of model grid spacing for typical midlatitude (Oklahoma) and tropical continental

106 (Amazon) conditions.

107

108 The 2-year measurements from the Green Ocean Amazon (GoAmazon) campaign provide

109 unprecedented data on the vertical velocity of deep convection by the Atmospheric Radiation

110 Measurement user facility (ARM, ARM Mobile Facility (AMF), Martin et al. 2017, Giangrande

111 et al. 2017). Recently, Giangrande et al. (2023) contrasted the thermodynamics and lifecycle

113 properties, including the vertical air velocity within isolated convective clouds observed during
114 the Amazon wet and dry seasons, and found that dry-season convection exhibited more intense
115 low-level updrafts and larger reflectivity associated with smaller convective cell areas than wet-
116 season counterparts. Dry-season convection also tended to exhibit a shorter life cycle and often
117 achieved maximum updraft and precipitation intensity at earlier life cycle stages than wet-season
118 storms. Pre-convective thermodynamics profiles from those events revealed that the dry season
119 showed a stronger deficit of dew-point temperature in the middle troposphere and higher values of
120 mean-layer convective available potential energy (MLCAPE) at lower levels.
121
122 In addition to primary thermodynamic transitions between wet and dry season convective regimes
123 (e.g., Giangrande et. al. 2020), the Amazon dry seasons may experience larger concentrations of
124 aerosols due to biomass burning that have been recently associated with potential secondary
125 contributions to changes in storm precipitation properties and convective vigor (e.g., Lin et al.
126 2006; Wang et al. 2018; Öktem et al. 2023). Moreover, the Amazon dry (wet) season has long
127 been suggested to promote a continental (maritime) convection contrast for a given
128 thermodynamic profile and background aerosols (Williams et al. 2002). Typical land-ocean
129 contrast is characterized by a "hot" continental surface (Williams and Stanfill 2002) and sea-breeze
130 type of mesoscale dynamics due to the thermal-patch effect (Robinson et al. 2011). Thus, instead
131 of focusing on the complex nature of land-ocean contrast or other active versus break monsoonal
132 contrasts performed globally (e.g., Holland et al. 1986, Keenan and Carbone 1992, Pope et al.
133 2009, Wu et al. 2009), the dry-wet season contrasts over the Amazon basin allows a unique
134 emphasis on the impact of thermodynamic profiles and large-scale dynamics upon the formulation
135 of convective vigor.
136
137 The main objective of this paper is to investigate dry-wet seasonal contrast and potential changes
138 in the evolution of deep convection cloud processes using an LES model and forward simulations
139 of Doppler radar observations. This attempts to reveal dynamical and microphysical processes that
140 explain the observed dry-wet contrasts, focusing on the bulk controls imposed by the background
141 thermodynamic profiles and large-scale forcing. The motivation for these efforts is the argument
142 that an improved understanding of these dry-wet contrasts should facilitate untangling the more
143 complex processes of land-ocean contrasts in deep convection. For this study, we employ a series

145 of daily large-eddy simulations (LESs) with bulk single-moment microphysics throughout the
146 GoAmazon campaign dry and wet season intensive observation periods (IOPs) to characterize dry-
147 wet season contrast in convection. These simulations are validated against the cumulative statistics
148 of ground-based Doppler velocity measurements during those periods. A thermal tracking analysis
149 is conducted to select golden cases from these dry- and wet-season LES runs to investigate the
150 physical process of convective vigor further. This effort focuses on thermodynamic impacts and
151 cloud dynamical roles in this manuscript, while the aerosol effects will be investigated in another
152 study.

153

154 Section 2 describes the general methodology and tools, including radar profilers, LES,
155 instrumental simulators, large-scale meteorological forcing, and thermal-tracking algorithms for
156 this study. Section 3 shows the results of the dry-wet contrast of meteorological forcing, statistical
157 composites of Doppler velocity, and thermal tracking analysis. Section 4 summarizes a thermal-
158 driven process of dry-season convective vigor, its uncertainties, and future directions.

159
160

161 **2.   Methods**

162

163 **2.1 GoAmazon: RWP Observations**

164

165 The primary datasets for this study are those collected by the 1290 MHz ARM Radar Wind Profiler
166 (RWP) operated during the U.S. Department of Energy's ARM ARM facility deployment during
167 its "Observations and Modeling of the Green Ocean Amazon 2014–2015" (GoAmazon) campaign
168 near Manaus, Brazil, from March 2014 through December 2015 (e.g., Martin et al., 2017). The
169 RWP was configured for precipitation sampling that included frequent vertical pointing to collect
170 conventional radar reflectivity factor Z and mean V_{dop} profiles through deep convective cells to
171 approximately 17 km in altitude (e.g., Giangrande et al. 2013, Giangrande et al. 2016, Wang et al.
172 2019, Williams et al. 2023). For measurements collected at these ultra-high frequencies and
173 without expectations for larger hail in Amazon deep convective storms (Liu and Zipser 2015, Bang
174 and Cecil 2019), all radar estimates are assumed as within Rayleigh scattering regimes, and
175 measurements are unattenuated in rain. The RWP deployed during GoAmazon had a beam width

177 of approximately 10 degrees thus horizontal measurement resolution is typically less than 1 km,

178 with a 200 m vertical (bin, gate) resolution and 10-s intervals between consecutive radar profiles.

179 All radar measurements were calibrated against a reference laser disdrometer collocated at the

180 main AMF site during the campaign (e.g., Wang et al. 2018), and a detailed method is discussed

181 in Williams et al. (2023).

182

183 For observation and simulation comparisons, the deep convective core is defined by using

184 thresholds applied to the observed and simulated RWP profiles: 1) column-maximum reflectivity

185 is greater than 35 dBZ, and 2) column-maximum V_{dop} is greater than 5 m/s. The choice for these

186 criteria is admittedly flexible, as model-vs-observed Z thresholds, in particular, are not necessarily

187 well-posed for convective-stratiform segregation such as removing all stratiform cells (e.g., Steiner

188 et al. 1995). Still, the additional velocity constraint afforded by the vertically-pointing RWP and

189 statistical representation of convective and stratiform composites seems to be reasonable (not

190 shown here), noting what is important is an attempt to apply thresholds for both observations and

191 simulations. A slightly different threshold does not alter the conclusions. Note that events on

192 3/19/14, 3/20/14, and 3/23/14, as well as the 10/4/14 cases from the dry season IOP, are clear

193 examples of Amazon mesoscale convective systems (MCSs, e.g., Wang et al. 2019). Thus, these

194 cases have also been removed from our statistical analysis to focus on isolated convective days.

195

196

197 **2.2 GoAmazon LES, Forcing, and Simulator**

198

199 GoAmazon LES runs utilize the Goddard Cumulus Ensemble (GCE), a cloud-process model

200 developed and improved at NASA GSFC over several decades (Tao *et al.* 2014). The GCE is

201 driven by large-scale forcing (LSF) with cyclic boundary conditions to generate cloud dynamics

202 and microphysics processes in Cartesian grid coordinates. No additional heat, moisture, or

203 momentum enters the domain apart from that imposed by the LSF or solar/infrared radiative

204 processes. In addition, GCE's anelastic dynamic core option allows faster integration of finer-

205 resolution runs (up to 1.5~2 times) than its compressible dynamic core option.

206

GoAmazon LES runs use 200-m horizontal grid spacing with 512 x 64 x 128 grids (x-y-z cartesian coordinates) with a 2-second model time step. Vertical grid spacings stretch from near surface level (starting from 44 m) and reach 200m around 4 km level, not to exceed horizontal resolution. Thus, the domain covers a 102 km x 12.8 km area; this "narrow channel" domain setup intends to resolve three-dimensional large eddies (i.e., thermals) while minimizing computational cost in order to run LES for the entire IOPs. In terms of model physics, the 1.5-order turbulent kinetic energy (TKE) scheme is used for subgrid turbulent mixing, and the Goddard radiation scheme is used for computing radiative flux and heating (Chou and Suarez 1999 & 2001, Matsui et al. 2018). The Goddard bulk one-moment 6-class scheme (4ICE hereafter) has four ice classes and uses preset size and density mapping for snow, graupel, and hail (Lang et al. 2014; Tao et al. 2016). 4ICE successfully generated a realistic L-O contrast of convective-core hydrometeor distributions compared to polarimetric radar retrievals in the previous study (Matsui et al. 2020). Also, note that the one-moment scheme is unaffected by the background aerosol concentrations to focus on the impact of thermodynamic and large-scale forcing on convective vigor in this study.

The LSF is derived from the VARiational ANALysis (VARANAL) approach, which is a broadly accepted method for generating large-scale forcing wherein data are collected and adjusted based on the vertical integration of the atmospheric mass, moisture, dry static energy, and momentum budgets (Zhang and Lin 1997, Zhang et al. 2001, Xie et al. 2004). The VARANAL approach is applied to the GoAmazon field campaign using ERA-Interim reanalysis (Dee et al., 2011) and constrained by radar-based surface precipitation rate (Tang et al. 2016). The horizontal/vertical advective forcings, mean wind profiles, and surface heat fluxes from the GoAmazon LSF are used to drive the LES. These fields are interpolated and imposed as tendency terms at every model time step. Our previous research demonstrated that GCE reproduced the observed precipitation quite well when forced by the GoAmazon LSF (Tao et al. 2022). GoAmazon LESs are run from September 2014 to 10 October 2014, defined as the dry-season IOP, and also run from 14 February 2014 to 26 March 2014, defined as wet-season IOP, as suggested by thermodynamic behaviors characteristic of larger dry and wet-season expectations, respectively (Giangrande et al. 2017, 2020). Each daily LES is initialized at 12 AM local time from the LSF and integrated just for 30 hours rather than continuously integrated during the entire IOPs because the convection life cycle typically follows a strong diurnal cycle due to the solar heating cycle, excepting propagating

238 organized convection (Tang et al. 2016, Giangrande et al. 2017, 2020). As a default setting, hourly
239 LES outputs are used to analyze the mean seasonal behavior of LESs.
240
241 Hourly LES outputs include an additional Doppler velocity field, corresponding to an expected
242 RWP observation through a multi-instrumental simulator, Goddard Satellite Data Simulator Unit
243 (G-SDSU, Matsui et al. 2014a; Matsui et al. 2014b). In this study, a ground-based Doppler radar
244 simulator is implemented in the model to replicate RWP observable signals. Radar backscatter is
245 estimated from nonRayleigh calculations with a Maxwell-Garnett assumption of air-water-ice
246 mixtures at 1290 MHz frequency, though for the RWP frequency, vertical pointing, and media
247 type/size expectations therein, the forward modeling is more straightforward than most weather
248 radar wavelength applications and appropriate for Rayleigh scattering assumptions. Doppler
249 velocity is estimated using pressure-adjusted hydrometeor terminal velocities weighted by radar
250 backscatter spectrum for each particle size distribution (PSDs). All these single scattering
251 calculations follow the 4ICE microphysics calculation/assumptions of particle size, density, and
252 phase for each hydrometeor species for physics consistency (Matsui et al. 2014b). Finally,
253 simulated signals are averaged consistent with the RWP beamwidth (10 degrees). This beamwidth
254 implies different averaging at different heights, for example, corresponding to six horizontal grids
255 of the LESs being averaged for a representative output at the 15 km height. Overall, this beamwidth
256 averaging smear LES-scale Doppler velocity signal statistics closer to the anticipated observed
257 instrumental signals (Matsui et al. 2014b). However, it should be noted that the exact sampling
258 methods are different between observations and simulations. For example, the RWP observations
259 are vertical pointing measurements that collect profiles at 6-second ("instantaneous") intervals. In
260 contrast, the modeled RWP signals are drawn from a domain-wide sampling of hourly LES outputs.
261
262
263 **2.3 Thermal Tracking Algorithm**
264
265 The thermal tracking method used here is described in detail by Hernandez-Deckers and Sherwood
266 (2016), who improved the initial version used by Sherwood et al. (2013). It is an offline algorithm
267 that uses high temporal resolution output (~1 min) from LES to identify and track coherent rising
268 volumes of cloudy air, i.e., thermals. The algorithm first identifies all peak vertical velocities larger

than 0.8 m/s that have water condensate content of at least 0.01 g/kg at every available snapshot of the simulation and matches peaks from successive snapshots to identify the available points of the trajectories of rising cloudy air parcels. A third-order polynomial is fitted to these points to reconstruct smooth trajectories and to allow a precise estimate of the ascent rate of the rising air volume at each snapshot. Notice that this ascent rate differs from the actual vertical velocity at a particular grid point since thermals develop internal toroidal circulations such that the peak vertical velocity at their centers is higher than the actual ascent rate of the air volume (e.g., Blyth et al. 2005; Sherwood et al. 2013).

The extent of each rising air volume (the size of each thermal) is estimated assuming a spherical shape centered at its smoothed trajectory, ensuring that the average vertical velocity of the enclosed volume matches that obtained from the derivative of the trajectory. Tracked thermals must fulfill certain requirements; for example, they must be tracked for at least three time steps, their radius must be larger than twice the horizontal grid spacing, their time-average ascent rate must be at least 1 m/s, their change in size in between successive snapshots must be less than 80% of the smallest radius, and most importantly, their trajectories must be consistent with their vertical momentum budget. The momentum budget of a tracked thermal is computed from its buoyancy (obtained from the density field), the pressure gradient force (obtained by integrating the pressure field over the entire thermal's surface), a "resolved mixing term" (obtained from the convergence of vertical momentum flux across the thermal's surface), and an entrainment or detrainment contribution due to the change in size between snapshots. This allows us to compute the expected final position of each thermal based only on its initial ascent rate, which is compared with the thermal's last tracked position. The distance between the actual and expected final positions must be smaller than the average thermal diameter and smaller than 20 % of the vertical distance traveled; otherwise, the thermal is discarded.

Once thermals are tracked with this algorithm, many properties can be studied based on all available model variables of interest. For example, average values for each thermal, such as ascent rate, size, altitude, entrainment rate, etc., are easily computed. Also, composites of different quantities can be obtained for different "stages" of a thermal's lifecycle. Typically, thermals exhibit one maximum ascent rate throughout their lifetime, which indicates their most vigorous phase.

300 This time step is used as a time reference common (t=0) to all thermals to create composites of

301 various properties at different stages of thermal lifetimes. Note that our tracking algorithm cannot

302 analyze merging or splitting thermals, regardless of their occurrence. This limitation requires

303 further study.

304

305 This thermal tracking algorithm was first used to study the main properties of cumulus thermals in

306 simulations of transient-growing convection (Sherwood et al., 2013; Hernandez-Deckers and

307 Sherwood, 2016) and provided strong evidence that thermals are typically small, short-lived (4-5

308 minutes on average), and mix vigorously with their environment. Also, Hernandez-Deckers and

309 Sherwood (2016) showed that the spherical shape approximation is generally valid and that

310 thermals, rather than plumes, are a more realistic building block for cumulus clouds. Hernandez-

311 Deckers and Sherwood (2018) used this algorithm to study the mixing properties of thermals in

312 more detail and contrast them with known parameterizations. Results from these studies have set

313 up the stage for a deeper understanding of cumulus dynamics and for further studies that use

314 different approaches (e.g., Gu et al., 2020; Morrison et al., 2020; Peters et al., 2020; Xu et al.,

315 2021; Morrison et al., 2023). Recently Hernandez-Deckers et al. (2022) used this algorithm to

316 study aerosol-deep convection interactions, highlighting the importance of the strong coupling

317 between microphysics and small-scale dynamics in convective clouds. Here we run this tracking

318 algorithm with the GCE model output for 5 hours starting at 1900Z (3 pm local time) on 09/07/14

319 (dry case) and 02/26/14 (wet case), using 1-minute interval output.

320

321

322 **3. Results**

323

324 **3.1 Dry-Wet Contrast of Large-Scale Forcing**

325 Campaign atmospheric thermodynamic profiles and the typical variability observed during

326 GoAmazon dry and wet seasons have been previously depicted using composite radiosonde skew-

327 T log-P diagrams (e.g., Giangrande et al., 2017, 2020, 2023). These depictions often show very

328 similar temperature profiles between dry and wet seasons, whereas the moisture profiles indicate

329 apparent differences, highlighting the mid-level deficit of the dew-point temperature profile in dry-

season composites. Since this study utilizes LSF to drive LESs, seasonal thermodynamics and dynamics are re-characterized by the LSF (Tang et al. 2016).

In Fig. 1, we plot a time series of apparent moisture sinks (Q2), vertical moisture advection, and parcel potential buoyancy profiles with surface precipitation rate from GoAmazon LSF for the IOPs. These time series of LSF profiles are integrated and contrasted in terms of Contoured Frequency by Altitude Diagrams (CFADs, Yuter and Houze 1995) as the dry and wet season IOPs (Figure 2).

Here, Q2 is the sum of changes in moisture content, horizontal moisture advection, and vertical moisture advection (Yanai et al. 1973), balanced with net condensation rate and turbulent transport of moisture vertical advection. Large Q2 corresponds to a large atmospheric moisture loss due to net condensation loss (i.e., precipitation). Large Q2 is associated with intervals with heavier or more widespread surface precipitation; thus, dry-IOP Q2 and surface precipitation are typically smaller than wet IOP (Fig. 1a-b). Similarly, Figs. 1c-d shows that peaks of vertical moisture advection term coincide with those peaks in the Q2 rate. Note that the Q2 rate in tropical environments is mainly contributed by the vertical moisture advection term rather than the horizontal advection term (not shown here). More importantly, positive (red shade) vertical moisture advection of the wet IOP tends to be stretched up to higher altitude (up to 200 mb) than the dry IOP (up to 600 mb) in most cases.

As previously discussed by Tang et al. (2016), the associated Amazon Q2 CFADs show the largest positive Q2 between 700 and 400 mb, while the largest negative Q2 is around 800 mb (Figs. 2a-b). The Dry-wet composite CFAD highlights more frequent positive Q2 values above the 800 mb level during the wet IOP. In contrast, more frequent negative Q2 during the dry IOP (Fig. 2c). Vertical moisture advection depicts similar CFAD shapes (Figs. 2d-e). Still, it highlights high frequencies of low-level positive vertical moisture advection and mid-to-low-level negative moisture vertical advection in the dry IOP in comparison with the wet IOP.

Finally, in Figs. 1e-f we plot the time series of parcel potential buoyancy profiles (positive components only), computed from LSFs by lifting surface airmass dry and moist adiabatically.

361 These potential buoyancy magnitudes are not necessarily associated with precipitation intensity.

362 Potential buoyancy CFADs show peak forcing between the 600 mb and 200 mb levels (Figs. 2g,

363 h, & i). The wet IOP suggests a larger variability of potential buoyancy at the upper troposphere

364 than the dry IOP (Figs. 2g-h). Potential buoyancy appears to be slightly stronger in the dry IOP,

365 and concentrated in a relatively lower troposphere than its wet IOP counterpart (Fig. 2i), which

366 agrees with findings in Giangrande et al. (2023). These results will be further discussed along the

367 thermal concentrations in the latter section.

368

369

370 **3.2 Dry-Wet Composite of Doppler Velocity CFADs**

371

372 Giangrande et al. (2023) highlighted dry-wet seasonal characteristics of storm vertical air motions

373 retrieved using RWP. They found that daytime isolated dry season convective cells tend to have

374 stronger updrafts at altitudes below the melting level. Yet, unlike their wet-season counterparts,

375 updrafts do not increase in intensity much above the melting layer. However, dry-season

376 convective cores were also characterized by stronger downdrafts at all altitudes, especially when

377 compared to wet-season counterparts aloft. Our present study utilizes similar direct measurements

378 of the mean V_{dop} from RWP to characterize the dry-wet contrast of deep convective cores. The

379 advantage of using V_{dop} measurements is that the quantity is the direct radar measurement and

380 helps reduce uncertainties from retrieval assumptions, such as requiring hydrometeor

381 identification or associated terminal fall speed corrections if the intent was to retrieve the vertical

382 air motion (Giangrande et al. 2013, 2016). Here, vertically-pointing V_{dop} measurements contain

383 sufficient information to evaluate storm characteristics, with the understanding that these

384 measurements represent the terminal velocities of hydrometeors combined with the vertical air

385 motion.

386

387 In Fig. 3a, we provide the cumulative sample numbers of CFADs (for each bin of V_{dop} and altitude)

388 as simulated and subsampled from the LES hourly outputs from the combined dry and wet season

389 IOPs. If the sampling numbers are normalized for each altitude, the Vdop CFADs will be formed.

390 Fig. 3b shows the sum of hydrometeor mass concentrations from each V_{dop}-altitude bin. Namely,

391 each hydrometeor mass concentrations from "cloud", "rain", "graupel-plus-hail", or "ice-plus-

393 snow" are separately accumulated for each bin. The larger number of samples associated with a

394 larger accumulated mass concentration of hydrometeor can generate the "representativeness" of

395 the hydrometeor class for a given V_{dop}-altitude bin location. Because V_{dop} is the sum of the vertical

396 velocity of the air and the terminal velocity of hydrometeor particles weighted by their reflectivity,

397 this plot facilitates understanding V_{dop} CFAD.

398

399 As mentioned above, we defined four regimes based on the accumulated mass of each hydrometeor

400 category. The "cloud" category (CL) is centered around -5 m/s of V_{dop} and 4 km altitude, slightly

401 overlapping with other categories. A "rain" category (RA) is more narrowly concentrated around

402 -8 m/s of V_{dop} and below 4 km altitude. The "graupel-plus-hail" category (GH) is centered around

403 -14 m/s of V_{dop} at 5 km altitude. Finally, an "ice-plus-snow" category (IS) is narrowly concentrated

404 along -1 m/s of V_{dop} above 5 km altitude. These locations roughly correspond to each hydrometeor

405 category's altitude and terminal velocity when factoring in the background/ambient vertical air

406 velocity. Note that our "cloud" regime has no terminal velocity in GCE 4ICE microphysics, thus

407 V_{dop} represents or tracks the background vertical air velocity and overlaps with the other regimes.

408 Moreover, simulated V_{dop} and hydrometeor statistics are also sensitive to model physics and those

409 assumptions to some degree. For example, any real-world cloud regime may be extended to higher

410 altitudes, but the model 4ICE microphysics scheme tends to quickly convert cloud liquid to cloud

411 ice category due to saturation adjustment (See Figs. 14-16 of Matsui et al. 2023). Nevertheless,

412 this representative mapping will help discuss the variability of the V_{dop} CFADs between the dry

413 and wet season IOPs.

414

415 In Fig. 4, we provide an observed and simulated climatology of V_{dop} CFADs as sampled from deep

416 convective cores and summarized over the dry and wet season IOPs. In both the dry and wet season

417 IOPs, the observed CFADs depict a smoother transition of the V_{dop} at the freezing level into the

418 melting layer (4-5 km, Figs. 4a-b). At the same time, simulations show a more abrupt transition

419 around the freezing layer (Figs. 4d-e). This is primarily because bulk single-moment microphysics

420 more abruptly converts solid to liquid phases through autoconversion than explicit bin-resolving

421 microphysics (Iguchi et al. 2014). This rapid conversion also overestimates the terminal velocity

422 of raindrops near and just below the freezing level. Another possible reason is overestimating the

423 graupel/hail size, leading to larger melted raindrops with high terminal velocity.

428

429   The CFADs have been summarized according to dry and wet season IOPs to explore these seasonal

430   contrasts between the deep convective cores (Figs. 4c, 4f). In the R regime (green box), the dry

431   IOP suggests more prevalent samples in strongly negative V_{dop} for our observations and

432   simulations, indicating that deep convective cores during the dry season IOP tend to have more

433   vigorous, faster-falling (larger) raindrops. In the GH regime (purple box), the dry season IOP

434   dominates the sampling. The observations indicate this dominance (red shade) up to 10 km altitude

435   (the extent that observations were included), while the simulation shows this behavior up to 8 km,

436   suggesting LES underestimation in graupel/hail altitudes. In the CL regime, the observations and

437   the simulations agree well, except that some sampling is overwhelmed by the dry season IOP

438   behaviors in the overlapped area. This likely indicates a shift in the presence of stronger low-level

439   updraft velocities, consistent with the analysis in Giangrande et al. (2023).

440

441   When considering the IS regime, there are examples of agreements and discrepancies between the

442   observations and simulations. One key agreement is that the wet IOP dominates the samples in the

443   area of positive V_{dop} above 8 km altitude. This indicates that observations and simulations suggest

444   a shift towards stronger upper-level vertical air velocity for the wet season IOP examples than for

445   the dry season IOP. This is consistent with the absence of dry mid-levels and the stochastic updraft

446   model expectations from Giangrande et al. (2023). On the other hand, the observations indicate a

447   more dominant sampling of velocities during the wet season IOP at around -3 m/s of V_{dop}, whereas

448   simulations change the dominant sampling mode from wet to dry IOPs at around 7 km altitude.

449   This is a potential bias in single-moment bulk microphysics, which tends to glaciate cloud droplets

450   or raindrops more quickly into ice particles than double-moment schemes (e.g., Fig. 16 of Matsui

451   et al. 2023). The observed composite also shows more dry-season dominant frequencies in GH

452   zones than the simulation, indicating the underestimation (overestimation) of raindrop/graupel

453   (ice/aggregate) particles above 7 km height.

454

455   Excepting this discrepancy in the IS regime, dry-wet composites of V_{dop} CFAD agree well between

456   observations and simulations, suggesting that LES could successfully represent the important

457   nature of dry-wet contrast, i.e., dry-season convection tends to generate stronger low-level updraft

459 velocity, generating more graupel/hail, and vigorous raindrops accompanied with stronger low-
460 level downdraft than the wet season.

461

462 To further investigate these seasonal shifts in core properties, golden cases are selected to analyze
463 deep convection lifecycle and processes. Golden cases are two single-day simulation cases, one
464 for dry and one for wet season, representing V_{dop} CFADs of each season. For this, the V_{dop} CFADs
465 are constructed for each day during the wet and dry season IOPs, and these daily CFADs are
466 compared to the composites of seasonal CFADs (not shown here). After day-to-day analysis of
467 correlation and root-mean-square errors between daily and seasonal CFADs, the convective event
468 on the 2/26/14 case is selected to represent the wet IOP convections. In contrast, the 9/7/14 case is
469 chosen to represent dry IOP convection. Fig. 5 shows a dry-wet composite of V_{dop} CFAD using
470 these two case studies. This figure compares quite well with the seasonal composite of V_{dop} CFAD,
471 having the dry convective vigor signals and model biases of the seasonal composite (Fig. 4f).

472

473 In Fig. 6, we show a time series of domain-mean profiles of convective cores drawn from these
474 dry- and wet-season golden cases, highlighting from 1600Z (1200 local time) of the starting day
475 to 0400Z (0000 local time) of the next day. The dry season golden event shows a clear diurnal
476 convection cycle, peaking at 2100-2200Z (local 5-6 pm). In contrast, the wet season golden event
477 shows an already ongoing, continuous sequence of deep convection with several embedded strong
478 pulses. Convective top heights reach up to 17 km for both the dry and wet events (Figs. 6a-b).
479 Low-level positive upward vertical velocity is more ubiquitous in the dry case, while upward
480 vertical velocity of the wet case extends to the middle-to-upper troposphere up to 15km (Figs. 6c-
481 d).

482

483 Dry-case graupel-plus-hail (GH) mass concentrations peak around 2100-2300Z when the
484 convective clouds reach their deepest cloud top heights, and the maximum GH concentration
485 exceeds that of the wet case. Rain mass concentrations peak between 2200Z and 00:30Z on the
486 subsequent day for the dry case, and this appears to be slightly more intense than the rainfall
487 simulated for the wet cases. Note that precipitation areal fraction is expected to be larger for the
488 wet season (i.e., Giangrande et al. 2016, 2023), such that dry-season convection is often
489 characterized by narrow yet intense isolated convection, while wet-season convection is

492   characterized by widespread moderate to deep convection (although with higher domain mass

493   flux). The intense surface rainfall rates are generally correlated with the generation of graupel,

494   frozen drops, and/or small hail particles during the dry-season convection, but there are some time

495   lags from 21Z to 22:50Z in the dry-case convection. This is because the initial convective core is

496   much narrower, and near-surface relative humidity is slightly low (~80%) around 21Z, and later

497   convective area increases so as near-surface relative humidity (~96%) around 21:50Z. Thus, more

498   surface rain evaporation likely suppresses surface precipitation during earlier convective periods.

499   These time series behaviors are generally consistent with the observed characteristics in the time-

500   integrated V_{dop} CFADs (Fig. 5).

501

502   One key question is why larger or heavily rimed particles tend to be preferentially generated in

503   dry-season convection compared to wet-season convection, given that both seasons indicate

504   convection with intense updraft velocity. This question follows previous efforts of Williams and

505   Stanfill (2002) for simulations of deep convection that contrasted land and oceanic clouds. For

506   example, while land and ocean environments may have similar convective available potential

507   energy (CAPE), differences in detailed potential buoyancy and vertical velocity profiles enable

508   additional graupel/hail particles to form in continental deep convection when compared to the

509   maritime environments (Matsui et al. 2020). A Lagrangian tracking analysis is performed to

510   examine this question for Amazon dry and wet season contrasts to investigate the dynamics and

511   microphysics within cumulus thermals for these dry and wet golden events (Section 3.3).

512

513

514   **3.3 Thermal Tracking Analysis**

515

516   Thermal tracking analysis (Section 2.3) was conducted over 5-hour periods from 1900Z to 0000Z

517   for the dry and wet season events using 1-minute LES outputs. Fig. 7 depicts normalized x-z cross-

518   sections of thermal properties at the moment of maximum vertical velocity in the dry and wet cases

519   and dry-wet differences. Thermals typically experience development and decaying stages in their

520   lifetime. During development, moist thermals increase their vertical velocity and size by releasing

521   latent heat and entraining surrounding air (Morrison et al. 2021). After defining and tracking each

522   thermal from the LESs, our normalizing procedure first defines the reference time from each

523 thermal's lifetime based upon peak vertical air velocity (denoted as thermal maxima) and then
524 conducts a weighting average of each thermal property at the thermal maxima only. Our weights
525 are based on the magnitude of thermal mass flux to avoid under-representing properties of less-
526 populated but vigorous thermals. Because these heights at thermal reference time are different for
527 each thermal in dry and wet case studies, averaging properties are somewhat biased toward thermal
528 vertical distributions (discussed later).

529

530 For example, in Fig. 7a we plot the weighted-average peak vertical air velocity (W) for the dry-
531 case thermal (9.6 m/s) and the wet-case thermal (10.6 m/s). Perhaps surprisingly, the flux- and
532 radius-weighted average dry-case thermal is slightly slower in W than that found for the average
533 wet-case. Here, we find that the vertical air velocity of the wet-case thermal is more
534 homogeneously distributed than its counterpart for the dry-case thermal, leading to higher
535 weighted-mean W despite weaker values at thermal centers (red shade in Dry-Wet plot, Fig. 7a).
536 Also, unexpectedly, supersaturation and cloud droplet mixing ratio (Qc) of the dry-case thermal
537 are elevated compared to the wet-case thermal (Fig. 6b-c), since wet-case thermals may be
538 expected to instead have higher supersaturation and/or more condensation owing to the higher
539 availability of water vapor (e.g., Giangrande et al. 2023).

540

541 Exploring the other classes, the rain mixing ratio (Qr) is similar between the dry-case and wet-case
542 thermals (0.17 g/kg), but graupel-hail concentrations (Qg+h) are significantly larger in the dry-
543 case thermals (0.95 g/kg) compared to the wet-case thermals (0.79 g/kg); this latter result is
544 consistent with previous discussions from event time-series in Fig. 6e. Cloud ice and snow mixing
545 ratio (Qi+s) values are slightly larger in the wet-case thermal (3.5 g/kg) than in the dry-case thermal
546 (3.2 g/kg). While this difference is not significant, this is also potentially a surprising outcome
547 since dry-case deep convective clouds might otherwise be expected to be deeper/stronger and thus
548 characterized by additional ice hydrometeor concentrations. However, some absence of these
549 media may be partially explained by following Giangrande et al. (2020; 2023) suggestions that
550 drier mid-to-upper levels in the dry season may limit periphery precipitation aloft (i.e., enhanced
551 evaporation). Overall, Qr and Qg+h seem to be concentrated in these composite averages
552 downward from the thermal core due to the gravitational sedimentation process. Supersaturation
553 and Qc, however, are also more vertically elongated than thermal properties established by

554 Hernandez-Deckers et al. (2022) using the Weather Research and Forecasting (WRF) model for a
555 case of scattered convection over Houston, Texas. Qi+s is more homogeneously distributed across
556 the defined borders of thermals. Also, dry-wet differences show slight asymmetric results,
557 particularly in W, Qr, and Qg+h. These could be attributable to differences in horizontal wind
558 shear, evidenced by a greater tilt in the thermal centerline flow in the dry case (gray streamlines),
559 leading to greater concentrations in the tilt direction of more rapidly sedimenting quantities that
560 are formed within thermals (i.e., Qr and Qg+h); since thermal composites are not aligned with the
561 mean wind, such preferential outflow may not be fully captured by this analysis (i.e., asymmetric
562 signatures could be greater or lesser along other directions than X alignment).

563

564 An initial leading question is why the dry-case thermals have greater cloud water and
565 supersaturation on average. To further untangle these results in Fig. 7b-c, we derive the vertical
566 profiles of flux-weighted mean thermal states, now including all thermal times (Fig. 8a-g).   **Deleted:** f
567 Immediately, these plots reveal striking differences between the thermal number concentration
568 (N) profiles for dry-case and wet-case examples (Fig. 8a; the number of thermals per km height
569 within the 102 km x 12.8 km domain). For instance, dry-case convection shows a larger
570 concentration of thermals below the 8 km height, while wet-case convection promotes a more
571 homogeneous thermal concentration that extends across most heights. This behavior is somewhat
572 reminiscent of the distribution for the difference in vertical moisture advection and potential
573 buoyancy profiles between the parent dry and wet season conditions (e.g., Fig. 1 and 2, discussions
574 in Section 3.1). Moreover, thermal generation in our LES responds to these terms partially from
575 the seasonal large-scale forcing.

576

577 According to the classic similarity theory of Morton et al. (1956), the width of dry/moist thermals
578 should increase with increases in the boundary layer depth (William and Stanhill 2002). For the
579 Amazon basin, previous GoAmazon studies such as Giangrande et al. (2017, 2023) showed that
580 dry season boundary layer height is generally deeper than that of the wet season, potentially on the
581 order of 200 m deeper for isolated deep convective events they tracked. Following this logic, dry-
582 case convection may anticipate larger thermals. However, LES thermal tracking analysis suggests
583 that the sizes (R) of thermals upon initiation appear to be quite similar between the wet and dry
584 events and then appear to grow at similar rates for several km before the dry-case thermal size

586 catches up with the moist size around 6 km in height, only to be overtaken again by the deeper

587 wet-case thermals around 9 km (Fig. 7b). Further, Fig. 8c shows the mean vertical velocity of

588 thermals, showing nearly identical updraft velocity below 4 km. However mean updraft velocity

589 profiles above 4 km are quite different between the dry and wet cases; e.g., the dry case peaks

590 around 8 km, while the wet case peaks at 6 and 10 km. This result implies that differences in moist

591 convection between dry and wet cases are poorly characterized by thermal sizes.

592

593 Qc in thermals also shows very similar profiles between the dry and wet cases (Fig. 8d). However,

594 because thermal numbers of the dry case are more concentrated at the lower troposphere (Fig. 8a),

595 all-height mean properties of dry-case thermals are characterized by more Qc (Fig. 7c). Qr of the

596 wet case is nearly twice as large as the dry case (Fig. 8e); however, normalized x-z cross-section

597 (Fig. 7d) does not show such a large difference (explained below). Qi+s also shows similar

598 distributions (Fig. 8f). Still, total x-z mean Qi+s is larger in the wet case than the dry case due to

599 larger thermal numbers in the upper troposphere (Fig. 7e). Uniqueness appears in thermal Qg+h

600 (Fig. 8g). While both dry and wet cases show similar magnitude of the peak values (~0.9 g/kg),

601 the peak height in the dry case is approximately 3 km higher than the wet case. This Qg+h peak of

602 the dry case coincides with the peak of vertical velocity (Fig. 8c).

603

604 Fig. 8h-k displays these hydrometeor mixing ratios averaged over the same periods, including all

605 convective grids defined by vertical velocity greater than 1 m/s. Vertical profiles and dry-wet

606 differences are similar to the results in Fig. 6. However, compared with the in-thermal profile

607 results (Fig. 8d-g), it facilitates understanding of the convective core microphysics process. First,

608 mean in-thermal convective-grid hydrometeor concentrations are smaller than in-thermal profiles;

609 particularly in-thermal Qc values are roughly six times larger than convective-grid average Qc

610 (Figs. 8d & 8h), suggesting that thermals are major cloud droplet generators (Hernandez-Deckers

611 et al. 2022).

612

613 The convective-grid Qg+h of the dry case is nearly twice as high as that in the wet case, peaked

614 around the melting layer (Figs. 8g & 8k), whereas in-thermal Qg+h shows similar peak values

615 between the dry and wet cases. As indicated by Fig. 7g, these larger and heavier rimed particles

616 sediment from thermals and further collision with supercooled liquid must enhance the graupel

Margin tracked-changes comments:

Deleted: perhaps better characterized by thermal numbers rather than thermal sizes.

Deleted: c

Deleted: d

Deleted: e

Deleted: f

Deleted: g
Deleted: j

Deleted: c
Deleted: f

Deleted: c
Deleted: g

Deleted: f
Deleted: j
Deleted: f
Deleted: ice and

growth during the sedimentation process, as suggested from aircraft measurements (Blyth and Latham 1993). Thus, elevated in-thermal Qg+h in dry-case convection can have further riming growth after falling out from thermals. This vigorous growth of Qg+h in dry-case convection eventually generates vigorous raindrops after the melting process. This could explain why convective-grid Qr in the dry case is larger than that in the wet case (Fig. 8i), opposite from the result of in-thermal Qr (Fig. 8e). Thus, in-thermal Qr values are not directly related to total Qr in the convective core (or surface precipitation rate) because of this cold precipitation microphysics process in deep convection.

A second leading question is why the height at the peak value of dry-case in-thermal Qg+h is more elevated than the wet-case thermal (Fig. 8g). Fig. 9 shows histograms of thermal properties from the dry and wet cases. Consistent with the mean vertical profiles (Fig. 8a), more thermals are initiated below 7 km in the dry case than in the wet case (Z0, Fig. 9d). Thermal radius in the wet case is also larger than the dry case regardless of shallower boundary layer depths in the wet case (Fig. 9a), consistent with R in thermal vertical profiles reaching larger sizes at most elevations in the wet case (Fig. 8b). However, here we see that thermal vertical velocity (W, Fig. 9b), travel distance (dZ, Fig. 9c), and lifetime (Fig. 9e) in the dry case are all greater than in the wet case. Thermal entrainment rate is smaller in the dry case than the wet case. These results indicate that the thermals in the dry-case deep convection can travel longer distances with an extended lifetime due to a lesser dilution.

Interestingly, slightly smaller thermal radii in dry-case convection can have a lower entrainment rate than in wet-case convection. Hernandez-Deckers and Sherwood (2018) also found that the variability of thermal radius can only account for 20% of the total variance of thermal dilution rate, i.e., larger thermal tends to have a lesser dilution rate. This was concluded through similar thermal tracking analysis from different LESs. Therefore, thermal size is not the sole parameter for determining dilution rate.

Giangrande et al. (2022) suggest that the convective area is smaller in dry-season convection over this region. Thus, this indicates that stronger low-level buoyancy in dry-season environments can more narrowly concentrate updraft and low-level thermals in the area, thus creating less diluted

669 environments probably due to the impact of thermal drag (Romps and Charn 2015). This is merely
670 speculative and requires further investigation to confirm or refute. Takahashi et al. (2022)
671 investigated cloud-scale entrainment between continental and maritime environments and found a
672 larger dilution rate in maritime convection than in continental convection. Our results suggest that
673 this difference in cloud dilution happens from the thermal-process level. These conditions elevate
674 dry-case thermals and graupel peak concentration toward higher altitudes than the wet-case
675 convection (Fig. 7f), leading to greater graupel production.
676
677 Finally, time series of thermal properties in the x-z cross-section are constructed for the dry case.
678 For this, each thermal at its maximum w value is centered and defined as the time of zero, and
679 prior (later) steps are represented in negative (positive) time steps. Because of the 1-minute LES
680 output, the time series from -3 to 3 encompasses 7 minutes of time steps. This averaging process
681 also weighs upon the magnitude of the thermal mass flux (Hernandez-Deckers et al. 2022); thus,
682 thermals at larger values in positive and negative time steps tend to have a fewer sampling numbers.
683 Also, to make the composites, equal-sized thermals are sampled to characterize the mean time
684 series of thermal properties, avoiding sampling too small thermals, which often has no
685 supersaturation (Hernandez-Deckers and Sherwood. 2016). This normalization procedure ends up
686 with the result that maximum W values do not appear at reference time (t=0), but better capture
687 the evolution of the largest flux-bearing thermals (Fig. 10). We also note that a typical thermal
688 travel distance is 1.3 km (Fig. 9c) and a minority of dry-case thermals therefore contain either no
689 ice phase (Fig. 8e-f) or no liquid phase (Fig. 8c-d), but most contain both phases between 3 and 7
690 km. Note that this flux-weighting is the one way to present the results, while simple non-weighting
691 averaging can also show similar results.
692
693 In the dry case (Fig. 10), within thermals that experience an extended peak in W ($6–11 \text{ m s}^{-1}$), the
694 average supersaturation, cloud, and rain mixing ratio peaks at the earlier steps and decreases
695 toward the end of the time steps. This indicates that a chunk of condensation heating is the main
696 initial driver of moist thermal growth. These thermal properties are typically centered around the
697 thermal core. By contrast, Q_{i+s} properties are more homogeneous and less concentrated at the core
698 of thermals, and they tend to increase toward the end of the time series. Especially, the early stages
699 (t=-3, -2, & -1) indicate thermals are approaching an existing ice layer rather than generating ice

702   around the thermal core. In the later stages (t=1, 2, & 3), the Qi+s is weakly concentrated toward

703   the upper thermal cores. This evolution of Qi+s suggests that thermals are not the main initiator of

704   Qi+s at the beginning, while Qi+s is rather entrained into the thermal within the early stages of the

705   mixed-phase zone, at least using the single-moment bulk microphysics. On the other hand, after

706   liquid saturation is no longer contributing substantially to Qc, Qi+s becomes a leading destination

707   of the overall transfer from vapor to hydrometeor phases within thermals that remain vigorous,

708   probably due to the Bergeron process (Bergeron 1935). Further research is needed to investigate

709   the ice nucleation and growth process in greater detail throughout the different stages of thermals'

710   lifecycle.

711

712   On the other hand, Qg+h increases toward the peak time of thermals (t=0), and starts decreasing

713   toward the later time steps (t=3). The spatial concentration of Qg+h is also peaked around the

714   thermal cores, similar to W, rh, Qc, and Qr. The increase of Qg+h coincided with the timing of

715   thermal entrapment of Qi+s and a reduction in Qc and Qr for time steps between -3 and 0. This

716   suggests that large concentrations of in-thermal Qc and Qr collide with entrained Qi+s to enhance

717   the riming process, generating graupel and hail particles at the thermal core. Note that the 4ICE

718   scheme only allows wet growth (collecting supercooled liquid) of graupel, while dry growth

719   (collecting ice and aggregate) of graupel has been suppressed due to unrealistic graupel in

720   convective anvil (Lang et al. 2014). After the reference time step (t=0), Qg+h decreases, most

721   likely due to sedimentation exceeding production. As indicated by Fig. 8g & 8k, this spilled

722   graupel and hail can further grow by colliding with supercooled liquid particles until melting.

723   Taken together, this analysis also suggests that this vigorous Qg+h-generation process in the

724   convective core *does not* occur through the classic parcel-driven convection. Instead, these graupel

725   and hail generations are most likely driven by sequential interactions of thermal ensembles and

726   microphysical processes. Note that the time series of the wet case also shows a similar finding but

727   is biased toward the thermals in the upper atmosphere (not shown here).

728

729   In addition to reference time, we composited thermal properties at different altitude levels (Fig.

730   11). The method for sampling and compositing is the same as in Fig. 10. However, it characterizes

731   vertical profiles of thermal composites using altitude references from 2.5km up to 10.5km,

732   including the mean air temperature. Despite of different reference methods, altitude-reference plots

---

Formatted: Font: (Default) Times New Roman, 12 pt
Formatted: Font: (Default) Times New Roman, 12 pt
Formatted: Font: (Default) Times New Roman, 12 pt
Formatted: Font: (Default) Times New Roman, 12 pt

Deleted: This also suggests that the glaciation process (i.e., conversion from supercooled liquid to ice hydrometeors) is usually completed after thermals vanish unless they reach the upper level of convective cores.

Formatted: Font: (Default) Times New Roman, 12 pt
Deleted: collision
Deleted: against
Deleted: and
Deleted: collision
Deleted: against
Deleted: is
Formatted: Font: (Default) Times New Roman, 12 pt
Deleted: .
Formatted: Font: (Default) Times New Roman, 12 pt
Deleted: f
Deleted: j
Deleted: and ice
Deleted: ; i.e., a large single air mass lifted from the cloud base up to the cloud top can generate latent heat and precipitation (Arakawa and Schubert 1974)

Deleted: .

appear to be similar patterns to time-reference plots. Vertical velocity (W) increases toward the peak level at 8.5 km, similar to the mean profile in Fig. 8c. There is strong supersaturation (S) between 4.5 km and 6.5 km, which rapidly decreases above 8.5 km. Qc, Qr, Qi+s, and Qg+h profiles also resemble thermal-mean profiles in Figs. 8d, 8e, 8f, and 8g, respectively. In thermal cores, Qc, Qr, and Qg+h are initially concentrated but sediment as thermals ascend. Even compared with the lifetime composite in Fig. 10, Qi+s are more stratified horizontally rather than toward thermal cores, particularly from 3.5 km to 6.5 km, suggesting entrainment of Qi+s within thermals at these altitudes. Simultaneously, Qc and Qr decrease while Qg+h increases at these altitudes. Because wet growth (ice collecting supercooled liquid) is the primary graupel growth process within 4ICE microphysics in the GCE (Lang et al. 2014), the droplet-loaded thermal penetration toward ice layers appears to be the important graupel/hail generation process within tropical deep convection.

4. Conclusion: Thermal-driven Convection Invigoration Process

We have investigated seasonal differences of the measured and simulated V_{dop} between the dry and wet seasons to confirm dry-season convective vigor associated with enhanced cold precipitation (graupel and hail) processes. Tracked thermal properties from the selected case studies reveal unique updraft microphysics processes in the convective core that explain the dry-wet contrast in deep convection. To summarize our findings in graupel-hail development sequences, a thermal-driven process is proposed in the following steps (Fig. 12a).

1. Where condensation may occur within moist turbulent structures in the lower atmosphere, local moist thermals may be initiated, which are characterized by dipole vortex rings with intense vertical velocity, supersaturation, cloud droplets, and raindrops around the thermal core.

2. When moist thermals penetrate the 0°C isothermal layer and dissipate in the mixed-phase zone, cloud droplets are detrained and gradually glaciated to form ice-particle layers.

3. As additional thermals fill with droplets at the thermal core and penetrate the glaciated mixed-phase zone, they entrain ice particles and collide with each other, generating graupel and hail embryos.

799   4. Once graupel and hail particles grow sufficiently large, they start falling out from thermals
800   and develop further by collecting supercooled droplets and ice particles during
801   sedimentation.
802
803   The process of generating ice layers (Step 3) could be the largest source of uncertainty in this study.
804   To prove the convective vigor process, this study used the simple bulk single-moment
805   microphysics parameterization (Lang et al. 2014, Tao et al. 2016). This parameterization tends to
806   convert droplets into ice particles through the saturation adjustment process. Cloud droplets are
807   glaciated much more quickly when compared to two-moment microphysics (e.g. Matsui et al.
808   2023). Time series as well as altitude reference composite also shows some ice generation within
809   the thermal core in later lifecycle stages (~10 km altitude), which may be associated with the
810   Bergeron process. Yet, ice crystal formation processes remain one of the largest sources of
811   microphysics uncertainty (Kanji et al. 2017; Korolev and Leisner 2020) and need further
812   investigation to establish with adequate parameterizations. Furthermore, updrafts passing through
813   the melting layer containing both large drops and ice crystals (which are identified here as a source
814   of graupel) have also been pinpointed as a leading source of secondary ice production in oceanic
815   convection sampled extensively via aircraft (Korolev et al. 2020). Thus, all quantitative
816   components of the proposed ice-graupel generation process described here remain uncertain and
817   subject to future investigations via instrumental observations and more detailed numerical
818   simulations.
819
820   Nonetheless, building on the ability of existing knowledge and simulations to reproduce some
821   basic features of observations during GoAmazon, Fig. 12b shows a newly proposed process that
822   can explain why dry-season convection has more graupel and intense precipitation than wet-season
823   counterparts in the following steps.
824   1. Dry-case (wet-case) convection tends to generate more (less) numbers of droplet-loaded
825   thermals from the lower atmosphere because of larger potential buoyant energy at a low
826   level in the dry season.
827   2. Once an ice layer is built from initial cumulus thermal ensembles (Fig. 11a), more (less)
828   numbers of droplet-loaded thermals penetrate ice layers to generate more (less) graupel and
829   hail embryos in dry-case (wet-case) convection.

Deleted: data
Deleted: near
Deleted: homogeneous freezing, vapor deposition or riming
Deleted: and
Deleted: ly
Deleted: e
Deleted: 1
Deleted: ¶

3. Individual dry-case (wet-case) thermals can rise to higher (lower) elevations via weaker (stronger) dilution with faster (slower) updraft, elevating in-thermal graupel at higher (lower) altitudes.

4. During sedimentation, graupel in dry-case (wet-case) thermals has a higher (lower) chance to grow due to the longer (shorter) distance toward the melting level.

These new processes are proposed from the "golden" cases from the dry and wet seasons. Further investigation with more case studies will augment our hypothesis in the future.

The "hotter" surface in the dry season must be the physical origin of step 1, similar to L-O contrast (William and Stanfill, 2002). The dry season typically has clearer skies, less soil moisture, and stronger surface heating, leading to more turbulent heat flux and energy at the lower troposphere even during GoAmazon experiment (Biscaro et al., 2021; Ghate and Kollias, 2016). In contrast, the wet season is characterized by frequent precipitation and increased release of atmospheric latent heat with the weak surface sensible heat flux caused by wet soil moisture (Rocha et al., 2004). As a result, the entire troposphere experiences upward motion during the wet season, unlike its dry season counterpart (Tang et al., 2016).

Contrary to the speculation made by William and Stanfill (2002), it has been found that stronger surface heating and deeper PBL during the dry season do not increase the thermal "size" based on the classic similarity theory of Morton et al. (1956). Instead, our analysis of simulations indicates that the numbers and updraft velocity profiles of cumulus thermals become more important, particularly those initiated in the lower troposphere. Even for similar CAPE, the concentration of potential buoyancy profiles in the lower troposphere can trigger more vigorous convection. This is similar to the difference between mid-latitude continental and tropical maritime environments, where the mid-latitude continental environment tends to have more potential buoyancy in the mid-to-lower troposphere, leading to continental convective vigor (Matsui et al., 2020). For this, we need to investigate boundary layer dry thermals and deep-convective moist thermal seamlessly between various continental and maritime environments.

It is also hypothesized that the low-altitude concentrated cumulus thermal trains could additionally enhance the cold precipitation process by improving the residence time of graupel and hail within

the mixed-phase zone if thermal-spilled graupel and hail encounter subsequent new cumulus thermals. Previous trajectory modeling (Heymsfield 1983) also suggested a similar mechanism for enhancing graupel and hail residence time and growth by multiple convective cores. Heymsfield (1983) used the multi-Doppler technique to generate a three-dimensional wind field, but it needed more spatio-temporal resolution to characterize cumulus thermal. However, a stronger updraft core mentioned in his study must be cumulus thermals. This investigation further requires a more complex set of numerical simulations in the future.

The proposed thermal-driven invigoration process is based solely on thermodynamics and does not consider aerosols' effect on deep convection, as demonstrated by previous studies over the Amazon (William et al. 2002, Lin et al. 2006). Our choice of single-moment microphysics does not consider the variability of background aerosols to initiate cloud droplets. However, this simple microphysics can generate a fundamental dry-wet contrast characterized by the V_{dop} statistics. This suggests that thermodynamics is the primary factor determining convective vigor, while aerosols may have a significant but secondary role in invigorating convection (Matsui et al. 2020). Future studies will require a higher-order moment of microphysics scheme to examine the impact of aerosols on droplet and primary ice nucleation in thermals to confirm our hypothesis that dry-wet aerosol contrast plays a secondary role.

It is well known that severe hailstorms and large hails are more frequently observed over the central plains of North and South America (Liu and Zipser 2015, Bang and Cecil 2019). The hailstorms in these regions are often associated with supercells, and mesocyclones play a crucial role in the growth of very large hail by enhancing the residence time of the hails within the mixed-phase zone (e.g., Nelson 1983; Ziegler et al. 1983). However, it is not known how a mesocyclone affects thermal-like or plume-like updraft characteristics (Morrison et al., 2020), though satellites have captured thermal chain-like periodic overshooting signals at the top of the supercells (Borque et al. 2020). Thus, further observational and modeling investigations are required for the mid-latitude regions to determine whether our proposed graupel/hail generation mechanisms can be applied.

The proposed process for graupel-hail generation and convective vigor is a time-dependent, sequential, coupled dynamics-microphysics process. Although the traditional plume-based mass

flux scheme has been successful in representing the moist convection process in climate models, (e.g., Arakawa and Schubert 1974), our proposed convective microphysics process is not linear and cannot be adequately represented by the traditional convective mass flux method. To represent this process, thermal chain concepts with detailed microphysics processes must be introduced in the parameterization for large-scale models (Morrison et al., 2020). Fine-resolution simulations produce better continental convective vigor because they can resolve thermal dynamics and microphysics (Robinson et al., 2011; Matsui et al., 2020). The mean radius of the tracked thermal in this study, conducted using a 200 m mesh LES, is around 1 km, with a maximum size of around 2 km, which is comparable to the LES study using a 65-m horizontal grid spacing (Hernandez-Deckers and Sherwood, 2016). However, due to the effective resolution being 5-10 times the actual grid spacing, cumulus thermals, and graupel-hail generation processes are difficult to resolve for storm-resolving models and perhaps any coarser Eulerian-type numerical atmospheric models (Matsui et al., 2016). Conducting LES for regional and global weather and climate models is impractical in the foreseeable future. Therefore, new types of dynamics-microphysics-coupled cumulus thermal parameterization should be developed to better represent deep convection for storm-resolving and coarse-resolution weather and climate models.

New ground-based Doppler phased array radar (PAR) technology (Kollias et al. 2022b) or multi-Doppler agile scans (Kollias et al. 2022a) hold promise in observing and characterizing cumulus thermals. Emerging PAR instruments have started capturing storm motion and microphysical details at spatial and temporal resolutions akin to those seen in LES output (e.g. Takahashi et al. 2019, Kikuchi et al. 2020). These new observational capabilities are necessary for refining the dynamics and microphysics in LESs, particularly in elucidating the process behind thermal-driven convective vigor. Moreover, the advent of vertical motion estimates from high-resolution space-based radars [EarthCARE, Wehr et al. 2023; Investigation of Convective Updrafts (INCUS), https://incus.colostate.edu; the Atmosphere Observing System (AOS), https://aos.gsfc.nasa.gov) will soon enable the global mapping of convective updrafts. These new satellite radar measurements will generate a comprehensive global catalog detailing convective vigor and the speed of intense thermals.

938   **Code Availability.** The GCE LES code, G-SDSU simulator code, and Python plotting codes used
939   in this manuscript are all available in the NCCS Data Portal
940   (https://portal.nccs.nasa.gov/datashare/cloudlibrary/PUB_DATA/GoAmazon_ACP/Code/).
941

942   **Data Availability.** The RWP measurements and VARNAL LSF data were available from the
943   Atmospheric Radiation Measurement (ARM) ARM Data Discovery
944   (https://adc.arm.gov/discovery/#/). These data were obtained from the ARM Mobile Facility
945   (AMF) at Manacapuru, Amazonas, Brazil, funded by A. U.S. Department of Energy (DOE) Office
946   of Science User Facility managed by the Biological and Environmental Research program. The
947   analysis data used in this manuscript is also available in the NCCS Data Portal
948   (https://portal.nccs.nasa.gov/datashare/cloudlibrary/PUB_DATA/GoAmazon_ACP/Data/)
949

950   **Author contribution.** T. Matsui designed and performed the GCE LESs, the V_{dop} forward
951   simulation, and the thermal tracking. D. Hernandez-Deckers developed the thermal tracking and
952   analysis code for the GCE LESs and prepared the V_{dop} figures for the thermal analysis. S.
953   Giangrande and T. Biscaro prepared RWP V_{dop} analysis. T. Matsui prepared the manuscript with
954   contributions from all co-authors.
955

956   **Competing interests.** At least one of the (co-)authors is a member of the editorial board of
957   Atmospheric Chemistry and Physics.
958

959   **Acknowledgments.** This project is funded by the NASA CloudSat and CALIPSO Science Team
960   (CCST) program (program manager: Dr. David Considine, grant number: 80NSSC21K1135). The
961   development of GCE is funded by the NASA GSFC Strategic Science resources (Associate
962   Director for Institutional Planning and Operation: Dr. Karen Mohr). We also thank the NASA
963   Advanced Supercomputing (NAS) Division and Center for Climate Simulation (NCCS) (Project
964   Manager T. Lee at NASA HQ) for providing the computational resources to conduct the GCE and
965   G-SDSU simulations, thermal tracking analysis, and stored model outputs. The authors thank an
966   anonymous reviewer for improving the manuscript.
967

References

969 **References**

970 Arakawa, A. and Schubert, W. H. (1974): Interaction of a cumulus cloud ensemble with the

971   large–scale environment, Part I, J. Atmos. Sci., 31, 674–701.

972 Bang, S. D., and D. J. Cecil, 2019: Constructing a Multifrequency Passive Microwave Hail

973   Retrieval and Climatology in the GPM Domain. J. Appl. Meteor. Climatol., 58, 1889–

974   1904, https://doi.org/10.1175/JAMC-D-19-0042.1.

975 Biscaro, T. S., Machado, L. A. T., Giangrande, S. E., and Jensen, M. P. (2021): What drives

976   daily precipitation over the central Amazon? Differences observed between wet and dry

977   seasons, Atmos. Chem. Phys., 21, 6735–6754, https://doi.org/10.5194/acp-21-6735-2021.

978 Blyth, A. M., S. G. Lasher-Trapp, and W. A. Cooper (2005): A study of thermals in cumulus

979   clouds, Quarterly Journal of the Royal Meteorological Society, 131, 1171–1190,

980   https://doi.org/10.1256/qj.03.180.

981 Borque, P., Vidal, L., Rugna, M., Lang, T. J., Nicora, M. G., & Nesbitt, S. W. (2020). Distinctive

982   Signals in 1-min Observations of Overshooting Tops and Lightning Activity in a Severe

983   Supercell Thunderstorm. *Journal of Geophysical Research: Atmospheres*, *125*(20),

984   e2020JD032856. https://doi.org/10.1029/2020JD032856

985 Chou, M.-D. and Suarez, M. J. (1999): A solar radiation parameterization for atmospheric

986   studies, NASA Tech. Rep. NASA/TM-1999-10460, vol 15, p 38,

987   https://ntrs.nasa.gov/archive/nasa/casi.ntrs.nasa.gov/19990060930.pdf.

988 Chou, M.-D. and Suarez, M. J. (2001): A thermal infrared radiation parameterization for

989   atmospheric studies, NASA/TM-2001-104606, vol 19, p 55,

990   https://ntrs.nasa.gov/archive/nasa/casi.ntrs.nasa.gov/20010072848.pdf.

992   Dolan, B., B. Fuchs, S. A. Rutledge, E. A. Barnes, and E. J. Thompson (2018): Primary Modes

993   of Global Drop Size Distributions, J. Atmos. Sci., 75, 1453–1476,

994   https://doi.org/10.1175/JAS-D-17-0242.1.

995   Emanuel, K. A., David Neelin, J., and Bretherton, C. S. (1994): On large-scale circulations in

996   convecting atmospheres, Q. J. R. Meteorol. Soc., 120, 1111–1143,

997   https://doi.org/10.1002/qj.49712051902.

998   Ghate, V. P. and Kollias, P. (2016): On the Controls of Daytime Precipitation in the Amazonian

999   Dry Season, J. Hydrometeorol., 17, 3079–3097, https://doi.org/10.1175/JHM-D-16-

1000   0101.1.

1001   Giangrande, S. E., Biscaro, T. S., and Peters, J. M. (2023): Seasonal controls on isolated

1002   convective storm drafts, precipitation intensity, and life cycle as observed during

1003   GoAmazon2014/5, Atmospheric Chemistry and Physics, 23, 5297–5316,

1004   https://doi.org/10.5194/acp-23-5297-2023.

1005   Giangrande, S. E., Feng, Z., Jensen, M. P., Comstock, J. M., Johnson, K. L., Toto, T., Wang, M.,

1006   Burleyson, C., Bharadwaj, N., Mei, F., Machado, L. A. T., Manzi, A. O., Xie, S., Tang,

1007   S., Silva Dias, M. A. F., de Souza, R. A. F., Schumacher, C., and Martin, S. T. (2017):

1008   Cloud characteristics, thermodynamic controls and radiative impacts during the

1009   Observations and Modeling of the Green Ocean Amazon (GoAmazon2014/5)

1010   experiment, Atmospheric Chemistry and Physics, 17, 14519–14541,

1011   https://doi.org/10.5194/acp-17-14519-2017.

1012   Giangrande, S. E., Toto, T., Jensen, M. P., Bartholomew, M. J., Feng, Z., Protat, A., Williams, C.

1013   R., Schumacher, C., and Machado, L. (2016): Convective cloud vertical velocity and

1014   mass-flux characteristics from radar wind profiler observations during GoAmazon2014/5,

1015   Journal of Geophysical Research: Atmospheres, 121, 12,891–12,913,

1016   https://doi.org/10.1002/2016JD025303.

1017 Giangrande, S. E., Wang, D., and Mechem, D. B. (2020): Cloud regimes over the Amazon

1018   Basin: perspectives from the GoAmazon2014/5 campaign, Atmospheric Chemistry and

1019   Physics, 20, 7489–7507, https://doi.org/10.5194/acp-20-7489-2020.

1020 Giangrande, S. E., E. P. Luke, and P. Kollias (2012): Characterization of Vertical Velocity and

1021   Drop Size Distribution Parameters in Widespread Precipitation at ARM Facilities,

1022   Journal of Applied Meteorology and Climatology, 51, 380–391,

1023   https://doi.org/10.1175/JAMC-D-10-05000.1.

1024 Giangrande, S. E., S. Collis, J. Straka, A. Protat, C. Williams, and S. Krueger (2013): A

1025   Summary of Convective-Core Vertical Velocity Properties Using ARM UHF Wind

1026   Profilers in Oklahoma, Journal of Applied Meteorology and Climatology, 52, 2278–2295,

1027   https://doi.org/10.1175/JAMC-D-12-0185.1.

1028 Grabowski, W. W. & Petch, Jon (2009): Deep Convective Clouds. Clouds in the Perturbed

1029   Climate System: Their Relationship to Energy Balance. 2. 197-215,

1030   https://doi.org/10.7551/mitpress/9780262012874.003.0009.

1031 Gu, J.-F., Plant, R. S., Holloway, C. E., and Muetzelfeldt, M. R. (2020): Pressure drag for

1032   shallow cumulus clouds: From thermals to the cloud ensemble, Geophysical Research

1033   Letters, 47, e2020GL090460, https://doi.org/10.1029/2020GL090460.

1034 Hartmann, D. L. (2016): Global Physical Climatology, 2nd ed., Academic Press, Cambridge,

1035   UK, ISBN: 978-0-12-328531-7, DOI: https://doi.org/10.1016/C2009-0-00030-0.

1036 Hernandez-Deckers, D. and Sherwood, S. C. (2016): A Numerical Investigation of Cumulus

1037 Thermals, Journal of the Atmospheric Sciences, 73, 4117–4136, DOI: 10.1175/JAS-D-

1038 15-0385.1.

1039 Hernandez-Deckers, D. and Sherwood, S. C. (2018): On the Role of Entrainment in the Fate of

1040 Cumulus Thermals, Journal of the Atmospheric Sciences, 75, 3911–3924, DOI:

1041 10.1175/JAS-D-18-0077.1.

1042 Hernandez-Deckers, D., Matsui, T., and Fridlind, A. M. (2022): Updraft dynamics and

1043 microphysics: On the added value of the cumulus thermal reference frame in simulations

1044 of aerosol-deep convection interactions, Atmospheric Chemistry and Physics, 22(2), 711–

1045 724, DOI: 10.5194/acp-22-711-2022.

1046 Heymsfield, A. J. (1983): Case Study of a Hailstorm in Colorado. Part IV: Graupel and Hail

1047 Growth Mechanisms Deduced through Particle Trajectory Calculations, J. Atmos. Sci.,

1048 40, 1482–1509, https://doi.org/10.1175/1520-0469(1983)040<1482:CSOAHI>2.0.CO;2.

1049 Holland, G. J., John, L., McBride, R. K., Smith, D. J., Jasper, D., and Keenan, T. D. (1986): The

1050 BMRC Australian Monsoon Experiment: AMEX, Bulletin of the American

1051 Meteorological Society, 67(12), 1466-1472, doi: 10.1175/1520-

1052 0477(1986)067<1466:TBAMEA>2.0.CO;2.

1053 Iguchi, T., Matsui, T., Tao, W., Khain, A., Phillips, V., Kidd, C., L'Ecuyer, T., Braun, S., and

1054 Hou, A. (2014): WRF-SBM simulations of melting layer structure in mixed-phase

1055 precipitation events observed during LPVEx, J. Appl. Meteor. Climatol., 53, 2710-2731,

1056 doi:10.1175/JAMC-D-13-0334.1.

1057 Jeyaratnam, J., Luo, Z. J., Giangrande, S. E., Wang, D., & Masunaga, H. (2021): A satellite-

1058 based estimate of convective vertical velocity and convective mass flux: Global survey

and comparison with radar wind profiler observations, Geophysical Research Letters, 48,

e2020GL090675, https://doi.org/10.1029/2020GL090675.

Kanji, Z. A., Ladino, L. A., Wex, H., Boose, Y., Burkert-Kohn, M., Cziczo, D. J., & Krämer, M.

(2017): Overview of Ice Nucleating Particles, Meteorological Monographs, 58, 1.1–1.33,

DOI: 10.1175/AMSMONOGRAPHS-D-16-0006.1.

Keenan, T. D. and Carbone, R. E. (1992): A Preliminary Morphology of Precipitation Systems In

Tropical Northern Australia, Q.J.R. Meteorol. Soc., 118: 283-326,

https://doi.org/10.1002/qj.49711850406.

Kikuchi, H. et al. (2020): Initial observations for precipitation cores with X-band dual polarized

phased array weather radar, IEEE Transactions on Geoscience and Remote Sensing,

58(5), 3657-3666, http://doi.org/10.1109/TGRS.2019.2959628.

Kollias, P., Luke, E. P., Tuftedal, K., Dubois, M., & Knapp, E. J. (2022): Agile Weather

Observations using a Dual-Polarization X-band Phased Array Radar, 2022 IEEE Radar

Conference (RadarConf22), New York City, NY, USA, pp. 1-6, doi:

10.1109/RadarConf2248738.2022.9764308.

Kollias, P., Luke, E., Tuftedal, K., Dubois, M., & Knapp, E. J. (2022): Agile weather

observations using a dual-polarization X-band phased array radar, 2022 IEEE Radar

Conf., New York, NY, IEEE, 1–6,

https://doi.org/10.1109/RadarConf2248738.2022.9764308.

Kollias, P., & Coauthors (2022): Science Applications of Phased Array Radars, Bull. Amer.

Meteor. Soc., 103, E2370–E2390, https://doi.org/10.1175/BAMS-D-21-0173.1.

Korolev, A., Heckman, I., Wolde, M., Ackerman, A. S., Fridlind, A. M., Ladino, L. A., Lawson,

R. P., Milbrandt, J., and Williams, E. (2020): A new look at the environmental conditions

favorable to secondary ice production, Atmos. Chem. Phys., 20, 1391–1429,

https://doi.org/10.5194/acp-20-1391-2020.

Korolev, A. and Leisner, T. (2020): Review of experimental studies of secondary ice production,

Atmos. Chem. Phys., 20, 11767–11797, https://doi.org/10.5194/acp-20-11767-2020.

Lang, S. E., Tao, W.-K., Chern, J.-D., Wu, D., & Li, X. (2014): Benefits of a fourth ice class in

the simulated radar reflectivities of convective systems using a bulk microphysics

scheme, J. Atmos. Sci., 71, 3583–3612, https://doi.org/10.1175/JAS-D-13-0330.1.

Lin, J. C., Matsui, T., Pielke Sr., R. A., & Kummerow, C. (2006): Effects of biomass burning-

derived aerosols on precipitation and clouds in the Amazon Basin: A satellite-based

empirical study, Journal of Geophysical Research, 111, D19204,

doi:10.1029/2005JD006884.

Liu, C., & Zipser, E. J. (2015). The global distribution of largest, deepest, and most intense

precipitation systems. *Geophysical Research Letters*, *42*(9), 3591-3595.

https://doi.org/10.1002/2015GL063776.

Lucas, C., Zipser, E. J., & Lemone, M. A. (1994): Vertical velocity in oceanic convection off

tropical Australia, J. Atmos. Sci., 51, 3183–3193, doi:10.1175/1520-

0469(1994)051,3183: VVIOCO.2.0.CO;2.

Martin, S. T., & Coauthors (2017): The Green Ocean Amazon Experiment (GoAmazon2014/5)

Observes Pollution Affecting Gases, Aerosols, Clouds, and Rainfall over the Rain Forest,

Bulletin of the American Meteorological Society, 98, 981–997, DOI: 10.1175/BAMS-D-

15-00221.1.

Matsui, T., & Mocko, D. M. (2014): Transpiration and Physical Evaporation: Regional and

Seasonal Variability Over the Conterminous United States, In Encyclopedia of Natural

1105   Resources, 1st Ed.; Wang, Y. Q., Ed.; Taylor & Francis Group: New York. 1086pp,

1106   ISBN 9781439852583 - CAT# K12418.

1107   Matsui, T., & Coauthors (2014a): Current and Future Perspectives of Aerosol Research at NASA

1108   Goddard Space Flight Center, BAMS Meeting Summary 95, ES203–ES207, doi:

1109   http://dx.doi.org/10.1175/BAMS-D-13-00153.1.

1110   Matsui, T., & Coauthors (2014b): Introducing multisensor satellite radiance-based evaluation for

1111   regional Earth System modeling, Journal of Geophysical Research, 119, 8450–8475,

1112   doi:10.1002/2013JD021424.

1113   Matsui, T., & Coauthors (2016): On the land-ocean contrast of tropical convection and

1114   microphysics statistics derived from TRMM satellite signals and global storm-resolving

1115   models, Journal of Hydrometeorology, 17, 1425-1445, doi:10.1175/JHM-D-15-0111.1.

1116   Matsui, T., & Coauthors (2018): Impact of Radiation Frequency, Precipitation Radiative Forcing,

1117   and Radiation Column Aggregation on Convection-Permitting West African Monsoon

1118   Simulations, Climate Dynamics, 1-21, https://doi.org/10.1007/s00382-018-4187-2.

1119   Matsui, T., & Coauthors (2020): Polarimetric Radar Characteristics of Simulated and Observed

1120   Intense Convective Cores for a Midlatitude Continental and Tropical Maritime

1121   Environment, J. Hydrometeor., 21, 501–517, https://doi.org/10.1175/JHM-D-19-0185.1.

1122   Matsui, T., & Coauthors (2023): Systematic validation of ensemble cloud-process simulations

1123   using polarimetric radar observations and simulator over the NASA Wallops Flight

1124   Facility, Journal of Geophysical Research: Atmospheres, 128, e2022JD038134,

1125   https://doi.org/10.1029/2022JD038134.

1126 Morrison, H., Peters, J. M., Varble, A. C., Hannah, W. M., & Giangrande, S. E. (2020). Thermal

1127   Chains and Entrainment in Cumulus Updrafts. Part I: Theoretical Description. Journal of

1128   the Atmospheric Sciences, 77, 3637–3660. [DOI: 10.1175/JAS-D-19-0243.1]

1129 Morrison, H., Jeevanjee, N., Lecoanet, D., & Peters, J. M. (2023). What controls the entrainment

1130   rate of dry buoyant thermals with varying initial aspect ratio?. Journal of the Atmospheric

1131   Sciences, [DOI: 10.1175/JAS-D-23-0063.1], in press.

1132 Morton, B. R., Taylor, G. I., & Turner, J. S. (1956): Turbulent gravitational convection from

1133   maintained and instantaneous sources. Proc. Roy. Soc. London, 234A, 1–23,

1134   https://doi.org/10.1098/RSPA.1956.0011.

1135 Nelson, S. P., 1983: The influence of storm flow structure on hail growth. *J. Atmos. Sci.*, 40,

1136   1965–1983, https://doi.org/10.1175/1520-0469(1983)040<1965:TIOSFS>2.0.CO;2.

1137 Öktem, R., Romps, D. M., & Varble, A. C. (2023). No Warm-Phase Invigoration of Convection

1138   Detected during GoAmazon. Journal of the Atmospheric Sciences, 80, 2345–2364. [DOI:

1139   10.1175/JAS-D-22-0241.1]

1140 Peters, J. M., Morrison, H., Varble, A. C., Hannah, W. M., & Giangrande, S. E. (2020). Thermal

1141   Chains and Entrainment in Cumulus Updrafts. Part II: Analysis of Idealized Simulations.

1142   Journal of the Atmospheric Sciences, 77, 3661–3681. [DOI: 10.1175/JAS-D-19-0244.1]

1143 Pielke, R. A. (2001). Influence of the spatial distribution of vegetation and soils on the prediction

1144   of cumulus convective rainfall. Rev. Geophys., 39, 151–177,

1145   doi:10.1029/1999RG000072.

1146 Pope, M., Jakob, C., & Reeder, M. J. (2009). Regimes of the North Australian Wet Season.

1147   Journal of Climate, 22, 6699–6715. [DOI: 10.1175/2009JCLI3057.1]

1149 Prein, A. F., Ge, M., Valle, A. R., Wang, D., & Giangrande, S. E. (2022). Towards a unified

1150   setup to simulate mid-latitude and tropical mesoscale convective systems at kilometer-

1151   scales. Earth and Space Science, 9. [DOI: 10.1029/2022EA002295]

1152 Ramos-Valle, A. N., Prein, A. F., Ge, M., Wang, D., & Giangrande, S. E. (2023). Grid spacing

1153   sensitivities of simulated mid-latitude and tropical mesoscale convective systems in the

1154   convective gray zone. Journal of Geophysical Research: Atmospheres, 128. [DOI:

1155   10.1029/2022JD037043]

1156 Robinson, F., Sherwood, S., Gerstle, D., Liu, C., & Kirshbaum, D. (2011). Exploring the land-

1157   ocean contrast in convective vigor using islands. J. Atmos. Sci., 68, 602–618,

1158   https://doi.org/10.1175/2010JAS3558.1.

1159 Rocha, H. R., Goulden, M., Miller, S. D., Menton, M. C., Pinto, L. D. V. O., Freitas, H. C., &

1160   Figueira, A. M. S. (2004). Seasonality of water and heat fluxes over a tropical forest in

1161   eastern Amazonia. Ecol. Appl., 14, 22–32.

1162 Romps, D. M., & Charn, A. B. (2015). Sticky Thermals: Evidence for a Dominant Balance

1163   between Buoyancy and Drag in Cloud Updrafts. J. Atmos. Sci., 72, 2890–2901,

1164   https://doi.org/10.1175/JAS-D-15-0042.1.

1165 Sherwood, S. C., Hernández-Deckers, D., Colin, M., & Robinson, F. (2013). Slippery Thermals

1166   and the Cumulus Entrainment Paradox. Journal of the Atmospheric Sciences, 70, 2426–

1167   2442, [DOI: 10.1175/JAS-D-12-0220.1]

1168 Steiner, M., Houze Jr., R. A., & Yuter, S. E. (1995). Climatological characterization of three-

1169   dimensional storm structure from operational radar and rain gauge data. Journal of

1170   Applied Meteorology, 34, 1978–2007.

Stephens, G. L., Vane, D. G., Boain, R. J., Mace, G. G., Sassen, K., Wang, Z., ... CloudSat

    Science Team (2002). The CloudSat mission and the A-Train: A new dimension of

    space-based observations of clouds and precipitation. Bull. Amer. Meteorol. Soc., 83,

    1771-1790, doi:10.1175/BAMS-83-12-1771.

Stolz, D. C., Rutledge, S. A., & Pierce, J. R. (2015). Simultaneous influences of thermodynamics

    and aerosols on deep convection and lightning in the tropics. J. Geophys. Res. Atmos.,

    120, 6207–6231, https://doi.org/10.1002/2014JD023033.

Sullivan, S. C., Voigt, A. (2021). Ice microphysical processes exert a strong control on the

    simulated radiative energy budget in the tropics. Commun Earth Environ 2, 137,

    https://doi.org/10.1038/s43247-021-00206-7

Takahashi, H., Luo, Z. J., & Stephens, G. L. (2017). Level of neutral buoyancy, deep convective

    outflow, and convective core: New perspectives based on 5 years of CloudSat data.

    Journal of Geophysical Research: Atmospheres, 122(5), 2958-2969.

Takahashi, H., Luo, Z. J., & Stephens, G. L. (2021). Revisiting the entrainment relationship of

    convective plumes: A perspective from global observations. Geophys. Res. Lett.,

    https://doi.org/10.1029/2020GL092349

Takahashi, N., et al. (2019). Development of multi-parameter phased array weather radar (MP-

    PAWR) and early detection of torrential rainfall and tornado risk. Journal of Disaster

    Research, 14(2), 235-247, http://doi.org/10.20965/jdr.2019.p0235

Tang, S., Xie, S., Zhang, Y., Zhang, M., Schumacher, C., Upton, H., Jensen, M. P., Johnson, K.

    L., Wang, M., Ahlgrimm, M., Feng, Z., Minnis, P., and Thieman, M. (2016). Large-scale

    vertical velocity, diabatic heating and drying profiles associated with seasonal and diurnal

1193   variations of convective systems observed in the GoAmazon2014/5 experiment. Atmos.

1194   Chem. Phys., 16, 14249–14264, https://doi.org/10.5194/acp-16-14249-2016.

1195 Tao, W.-K., Lang, S., Zeng, X., Li, X., Matsui, T., Mohr, K., Posselt, D., Chern, J., Peters-

1196   Lidard, C., Norris, P. M., Kang, I.-S., Choi, I., Hou, A., Lau, K.-M., and Yang, Y.-M.

1197   (2014). The Goddard Cumulus Ensemble model (GCE): improvements and applications

1198   for studying precipitation processes. Atmospheric Research, 143, 392-424. doi:

1199   http://dx.doi.org/10.1016/j.atmosres.2014.03.005.

1200 Tao, W.-K., Wu, D., Lang, S., Chern, J.-D., Peters-Lidard, C., Fridlind, A., and Matsui, T.

1201   (2016). High-resolution NU-WRF simulations of a deep convective-precipitation system

1202   during MC3E: Further improvements and comparisons between Goddard microphysics

1203   schemes and observations. J. Geophys. Res. Atmos., 121, 1278–1305,

1204   https://doi.org/10.1002/2015JD023986.

1205 Tao, K., Iguchi, T., Lang, S., Li, X., Mohr, K., Matsui, T., & Braun, S. (2022). Relating Vertical

1206   Velocity and Cloud/Precipitation Properties: A Numerical Cloud Ensemble Modeling

1207   Study of Tropical Convection. *Journal of Advances in Modeling Earth*

1208   *Systems*, *14*(9), e2021MS002677. https://doi.org/10.1029/2021MS002677

1209 Tokay, A., and Short, D. A. (1996). Evidence from Tropical Raindrop Spectra of the Origin of

1210   Rain from Stratiform versus Convective Clouds. Journal of Applied Meteorology and

1211   Climatology, 35, 355–371. [DOI: 10.1175/1520-

1212   0450(1996)035<0355:EFTRSO>2.0.CO;2]

1213 Wang, D., Giangrande, S. E., Bartholomew, M. J., Hardin, J., Feng, Z., Thalman, R., and

1214   Machado, L. A. T. (2018). The Green Ocean: precipitation insights from the

GoAmazon2014/5 experiment. Atmospheric Chemistry and Physics, 18, 9121–9145.

[DOI: 10.5194/acp-18-9121-2018]

Wang, D., Giangrande, S. E., Schiro, K., Jensen, M. P., & Houze, R. A. (2019). The

characteristics of tropical and midlatitude mesoscale convective systems as revealed by

radar wind profilers. Journal of Geophysical Research: Atmospheres, 124, 4601–4619.

[DOI: 10.1029/2018JD030087]

Wehr, T., Kubota, T., Tzeremes, G., Wallace, K., Nakatsuka, H., Ohno, Y., Koopman, R., Rusli,

S., Kikuchi, M., Eisinger, M., Tanaka, T., Taga, M., Deghaye, P., Tomita, E., and

Bernaerts, D. (2023). The EarthCARE mission – science and system overview. Atmos.

Meas. Tech., 16, 3581–3608, https://doi.org/10.5194/amt-16-3581-2023.

Williams, E., and Stanfill, S. (2002). The physical origin of the land–ocean contrast in lightning

activity. C. R. Phys., 3, 1277–1292, doi:10.1016/S1631-0705(02)01407-X.

Williams, E., Chan, T., and Boccippio, D. (2004). Islands as miniature continents: Another look

at the land–ocean lightning contrast. J. Geophys. Res., 109, D16206,

doi:10.1029/2003JD003833.

Williams, E., Mushtak, V., Rosenfeld, D., Goodman, S., and Boccippio, D. (2005).

Thermodynamic conditions favorable to superlative thunderstorm updraft, mixed phase

microphysics and lightning flash rate. Atmos. Res., 76, 288–306,

doi:10.1016/j.atmosres.2004.11.009.

Williams, C. R., Barrio, J., Johnston, P. E., Muradyan, P., and Giangrande, S. E. (2023).

Calibrating radar wind profiler reflectivity factor using surface disdrometer observations.

Atmospheric Measurement Techniques, 16, 2381–2398. [DOI: 10.5194/amt-16-2381-

2023]

Wu, J., Del Genio, A. D., Yao, M.-S., and Wolf, A. B. (2009). WRF and GISS SCM simulations
of convective updraft properties during TWP-ICE. Journal of Geophysical Research, 114,
D04206. [DOI: 10.1029/2008JD010851]

Xie, S., Cederwall, R. T., and Zhang, M. (2004). Developing long-term single-column
model/cloud system–resolving model forcing data using numerical weather prediction
products constrained by surface and top of the atmosphere observations. J. Geophys.
Res., 109, D01104, doi:10.1029/2003JD004045.

Xu, X., Sun, C., Lu, C., Liu, Y., Zhang, G. J., and Chen, Q. (2021). Factors affecting entrainment
rate in deep convective clouds and parameterizations. Journal of Geophysical Research:
Atmospheres, 126, e2021JD034881. [DOI: 10.1029/2021JD034881]

Yanai, M., Esbensen, S., and Chu, J. (1973). Determination of Bulk Properties of Tropical Cloud
Clusters from Large-Scale Heat and Moisture Budgets. J. Atmos. Sci., 30, 611–627,
https://doi.org/10.1175/1520-0469(1973)030<0611:DOBPOT>2.0.CO;2.

Yuter, S. E., and Houze Jr., R. A. (1995). Three-dimensional kinematic and microphysical
evolution of Florida cumulonimbus. Part II: Frequency distribution of vertical velocity,
reflectivity, and differential reflectivity. Monthly Weather Review, 123, 1941–1963.

Zipser, E. J., Liu, C., Cecil, D. J., Nesbitt, S. W., and Yorty, D. P. (2006). Where are the most
intense thunderstorms on Earth? Bull. Amer. Meteor. Soc., 87, 1057–1071,
doi:10.1175/BAMS-87-8-1057.

Zhang, M., and Lin, J. (1997). Constrained variational analysis of sounding data based on
column-integrated budgets of mass, heat, moisture, and momentum: Approach and
application to ARM measurements. J. Atmos. Sci., 54(11), 1503–1524,
doi:10.1175/1520-0469(1997)054<1503:CVAOSD>2.0.CO;2.

Formatted: Font: (Default) Times New Roman

1261 Zhang, M., Lin, J., Cederwall, R. T., Yio, J. J., and Xie, S. C. (2001). Objective analysis of ARM

1262   IOP data: Method and sensitivity. Mon. Weather Rev., 129(2), 295–311,

1263   doi:10.1175/1520-0493(2001)129<0295:OAOAID>2.0.CO;2.

1264 Ziegler, C. L., P. S. Ray, and N. C. Knight, 1983: Hail growth in an Oklahoma multicell storm. *J.*

1265   *Atmos. Sci.*, 40, 1768–1791, https://doi.org/10.1175/1520-

1266   0469(1983)040<1768:HGIAOM>2.0.CO;2.

1267

1268

1269

1270 **Figures**
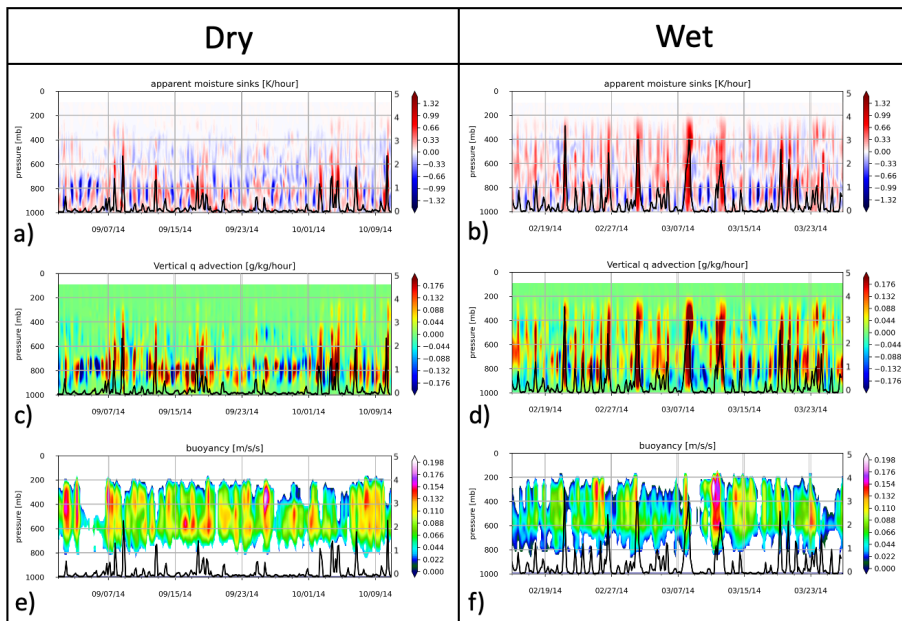
1271

1272 Figure 1. Time series of VARNAL large-scale forcing profiles between wet and dry periods: (a-b)
1273 apparent moisture sink (Q2), (c-d) vertical moisture advection, (e-f) potential buoyancy. The black
1274 solid lines on the secondary y-axis represent the surface precipitation rate.
1275
1276
1277
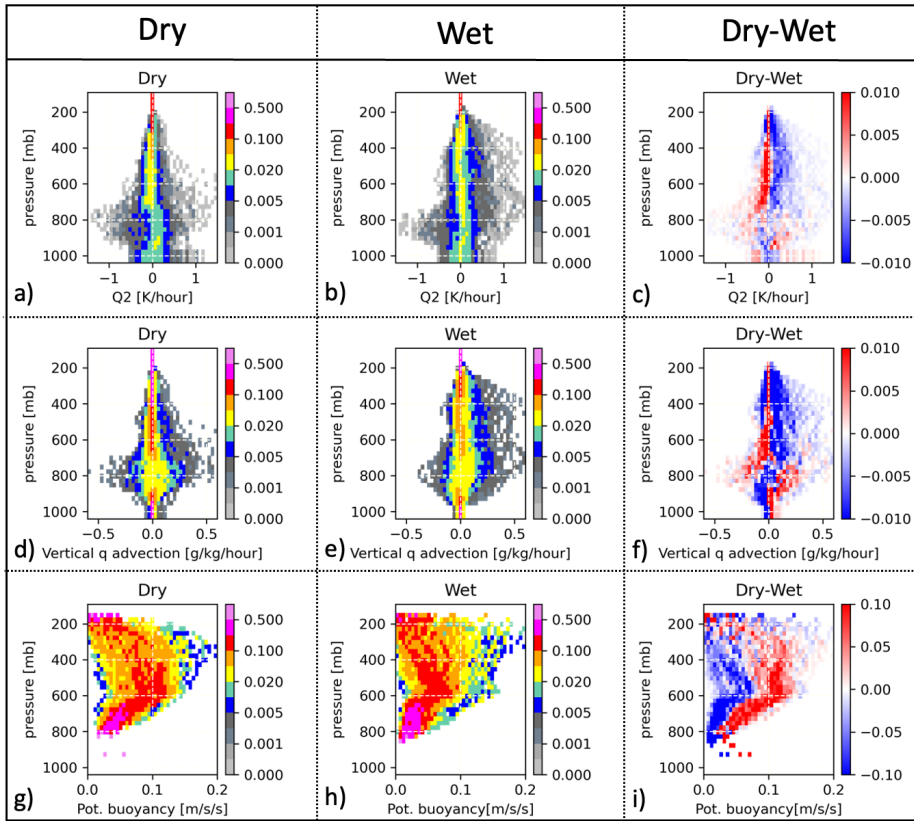
1278

1279 Figure 2. Contoured Frequency of Altitude Diagram (CFADs) of (a-c) apparent moisture sink (Q2),
1280 (d-f) vertical moisture (q) advection, (g-i) potential buoyancy integrated over dry and wet periods,
1281 as well as dry-wet differences.

1282

1283

1284
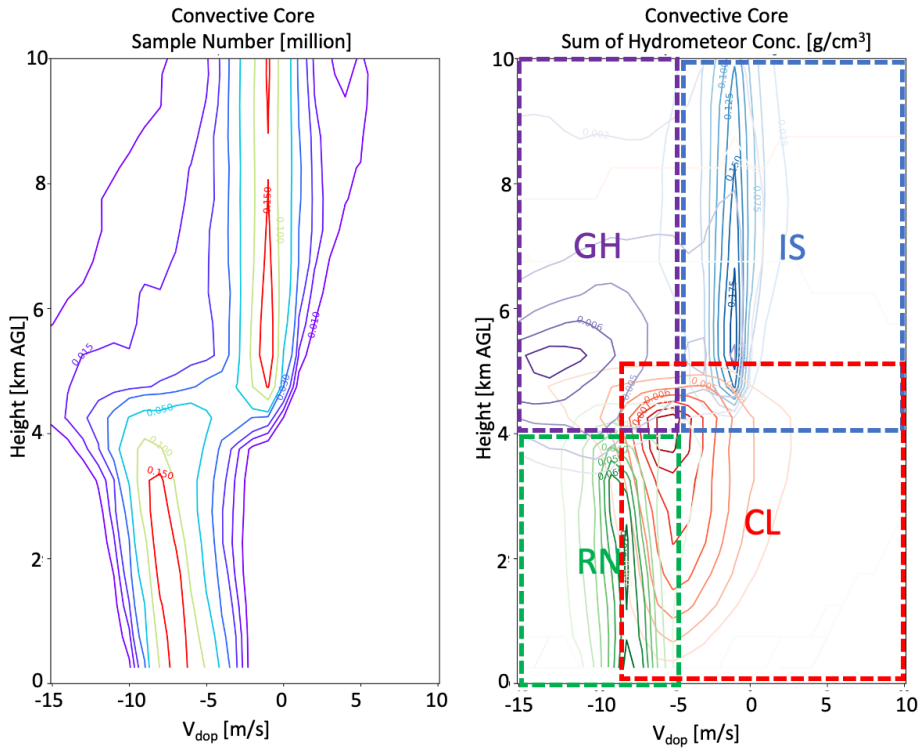
1287 Figure 3. (a) Cumulative V_{dop} sample numbers from LESs during dry and wet periods, presented
1288 as CFADs for each V_{dop} bin and altitude. (b) the cumulative hydrometeor mass concentrations
1289 from each V_{dop}-altitude bin. Red contours represent "cloud (CL)", green contours represent "rain
1290 (RN)" blue contours represent "ice and snow (IS)", and purple contours represent "graupel and
1291 hail (GH)".

1292

1293

1294

1295
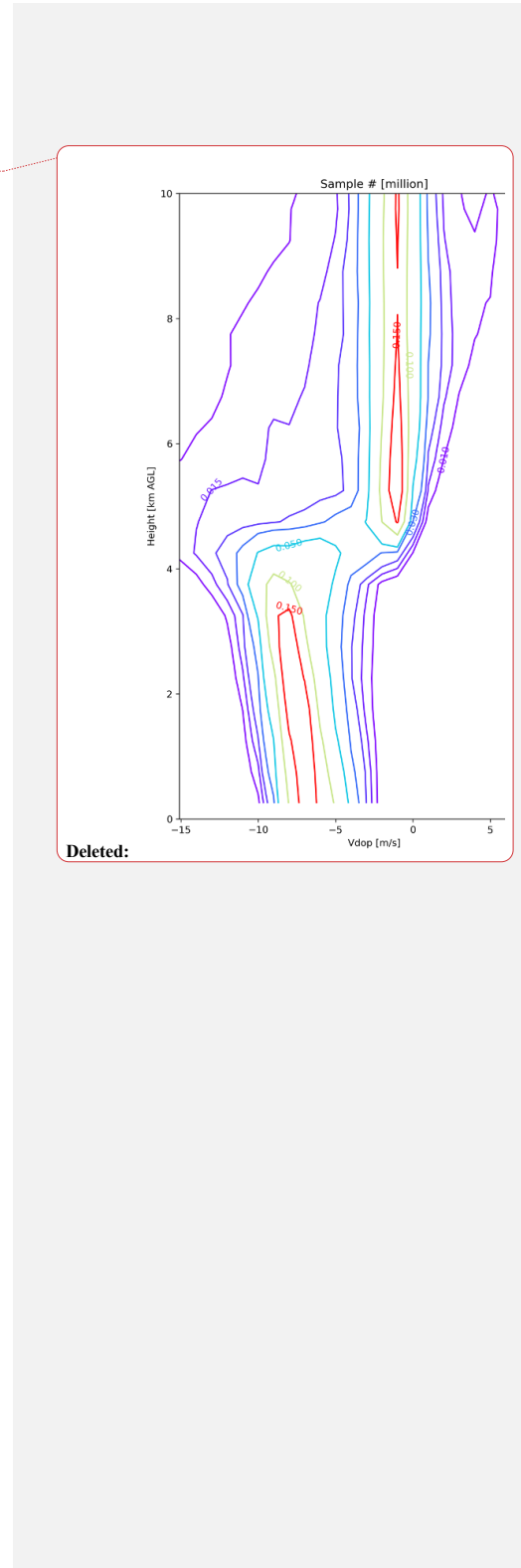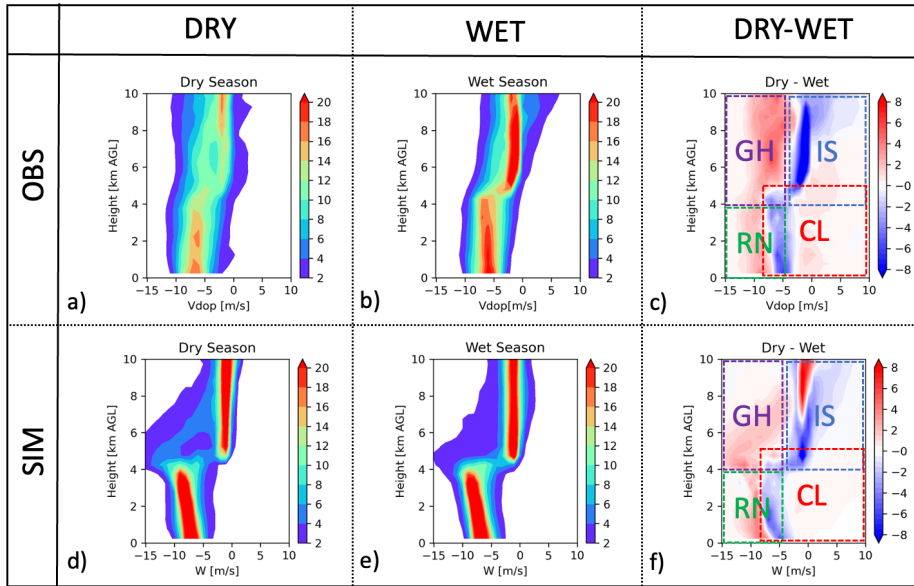
Figure 4. Contoured Frequency of Altitude Diagram (CFADs) of V_{dop} integrated over dry and wet periods, as well as dry-wet differences. The upper raw (a-c) represents observed composites, while the lower raw represents simulated composites. CL, RN, IS, and GH represent the hydrometeor regimes defined in Fig. 3.

1305
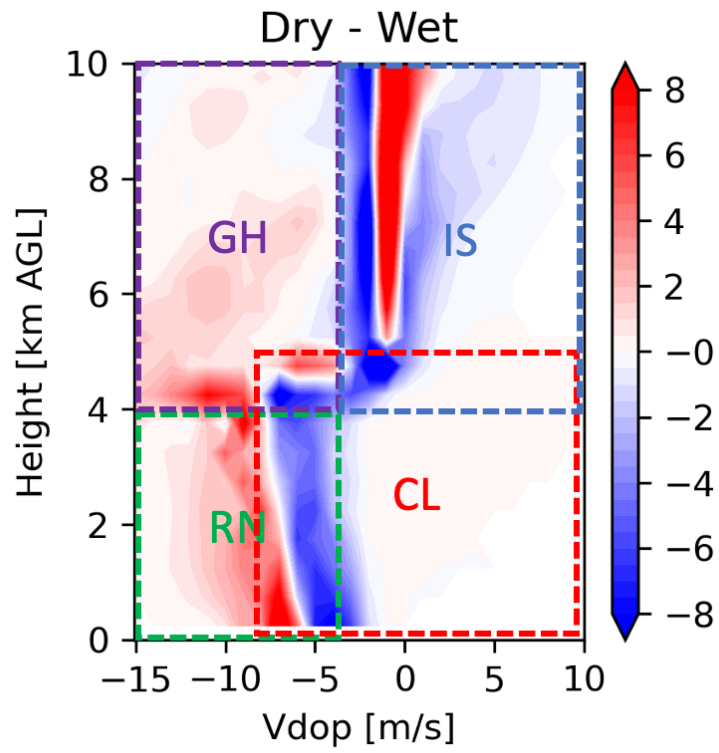
Figure 5. Contoured Frequency of Altitude Diagram (CFADs) of simulated V_{dop}, differentiated for
dry- and wet-season golden cases.

1306
1307
1308
1309
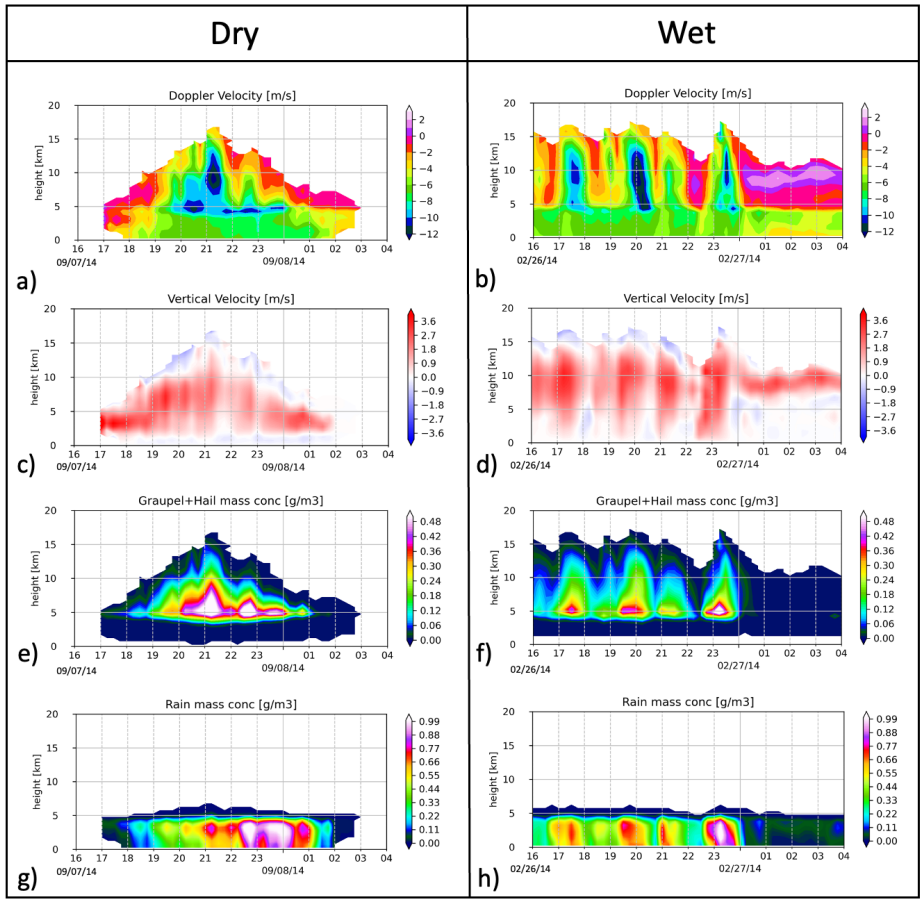
1310

1311 Figure 6. Time series of convective core-mean (a-b) Doppler velocity, (c-d) vertical velocity, (e-
1312 f) graupel and hail concentrations, and (g-h) rain concentrations profiles of convective grids from
1313 the dry- and wet-season golden cases.

1314

1315
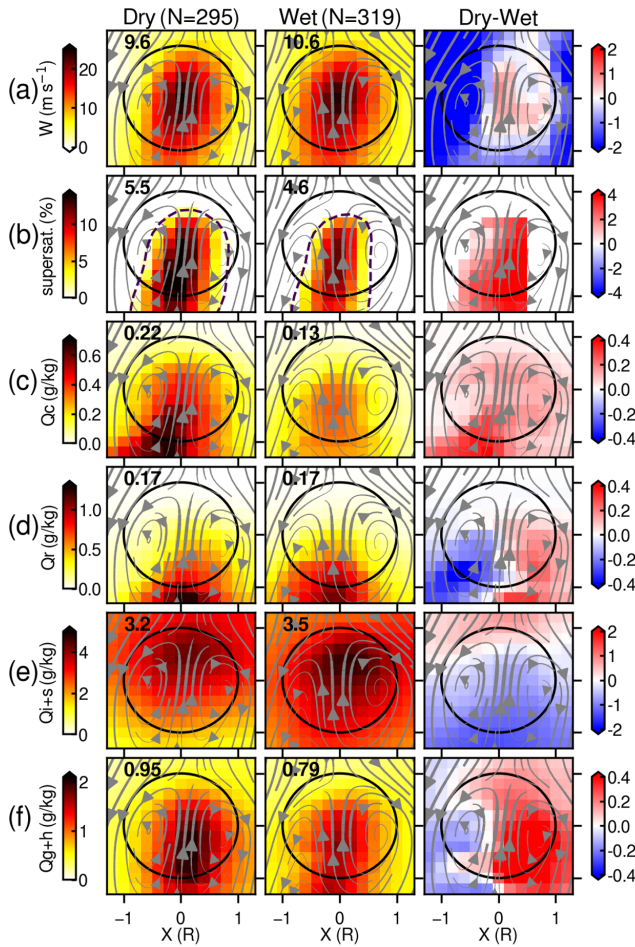
1317

Figure 7. Cross sections along the x-z plane of flux-weighted thermal values of (a) vertical velocity (W), (b) supersaturation (S), (c) cloud droplet mass concentration (Qc), (d) rain mass concentration (Qr), (e) ice and snow mass concentration (Qi+s), and (f) graupel and hail mass concentration (Qg+h), for composites of all tracked thermals at the point of their maximum vertical velocity, scaled by their radius (horizontal and vertical coordinates are in units of mean thermal radii). Left, middle, and right column corresponds to the dry-season golden case, the wet-season golden case, and dry-wet case difference, respectively. Upper left values in each panel are the flux- and radius-weighted mean over all samples. Arrows indicate the average flow streamlines in the rising thermal reference frame. The dashed contour in supersaturation values corresponds to 100% relative humidity. These are reference-time (t=0) mean values.

1318
1319
1320
1321
1322
1323
1324
1325
1326
1327
1328

1329
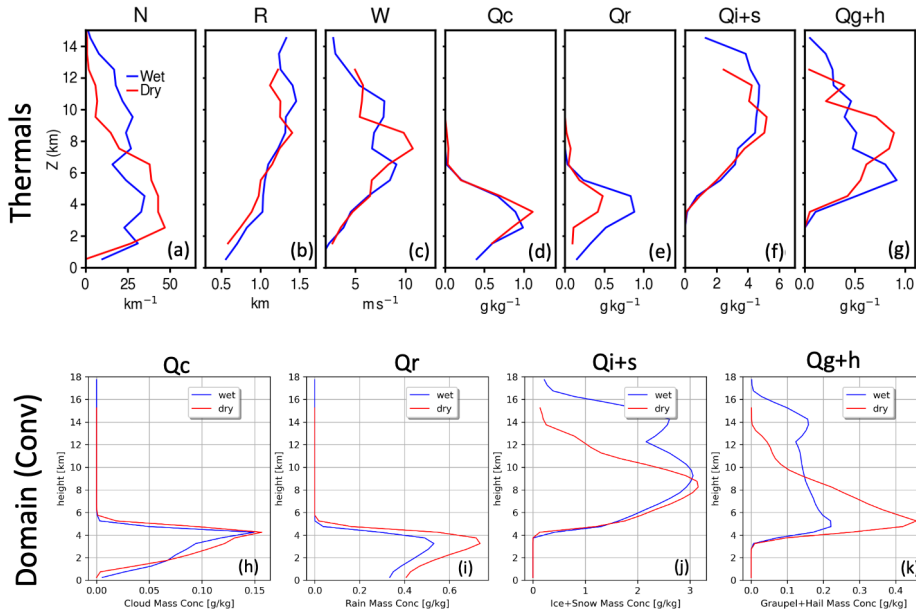
1330

1331 Figure 8. (a-f) Vertical profiles of thermal-mean (a) number concentrations (N), (b) radius (R), (c)
1332 vertical velocity (W), (d) cloud droplet mass concentration (Qc), (e) rain mass concentration (Qr),
1333 (f) ice and snow mass concentration (Qi+s), and (g) graupel and hail mass concentration (Qg+h).
1334 These are all-thermal mean values.
1335 (g-j) Vertical profile of domain-mean (h) cloud droplet mass concentration (Qc), (i) rain mass
1336 concentration (Qr), (j) ice and snow mass concentration (Qi+s), and (k) graupel and hail mass
1337 concentration (Qg+h)   of convective grids from the dry- and wet-season golden cases.

1338

1339
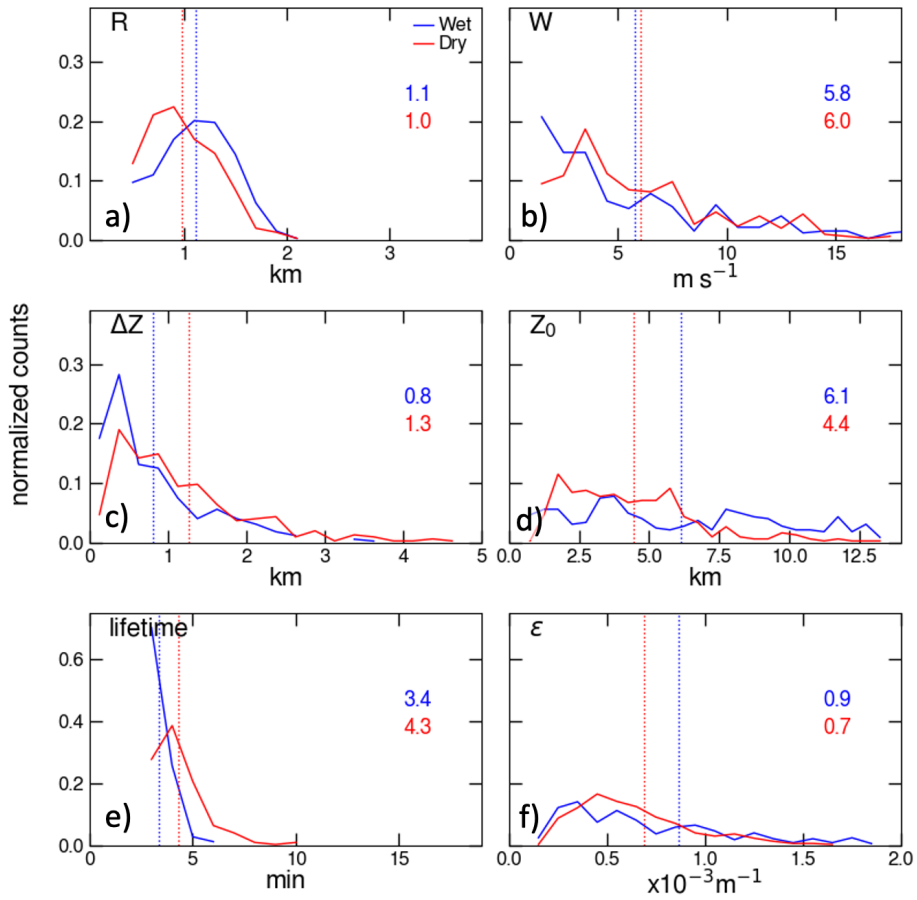
1348
1349   Figure 9. Normalized histogram of thermal (a) radii (R), (b) vertical velocity (W), (c) travel
1350   distance (ΔZ), (d) initiated level (Z_0), (e) lifetime, and (f) entrainment rate (ε) from the dry- and
1351   wet-season golden cases.
1352

1353
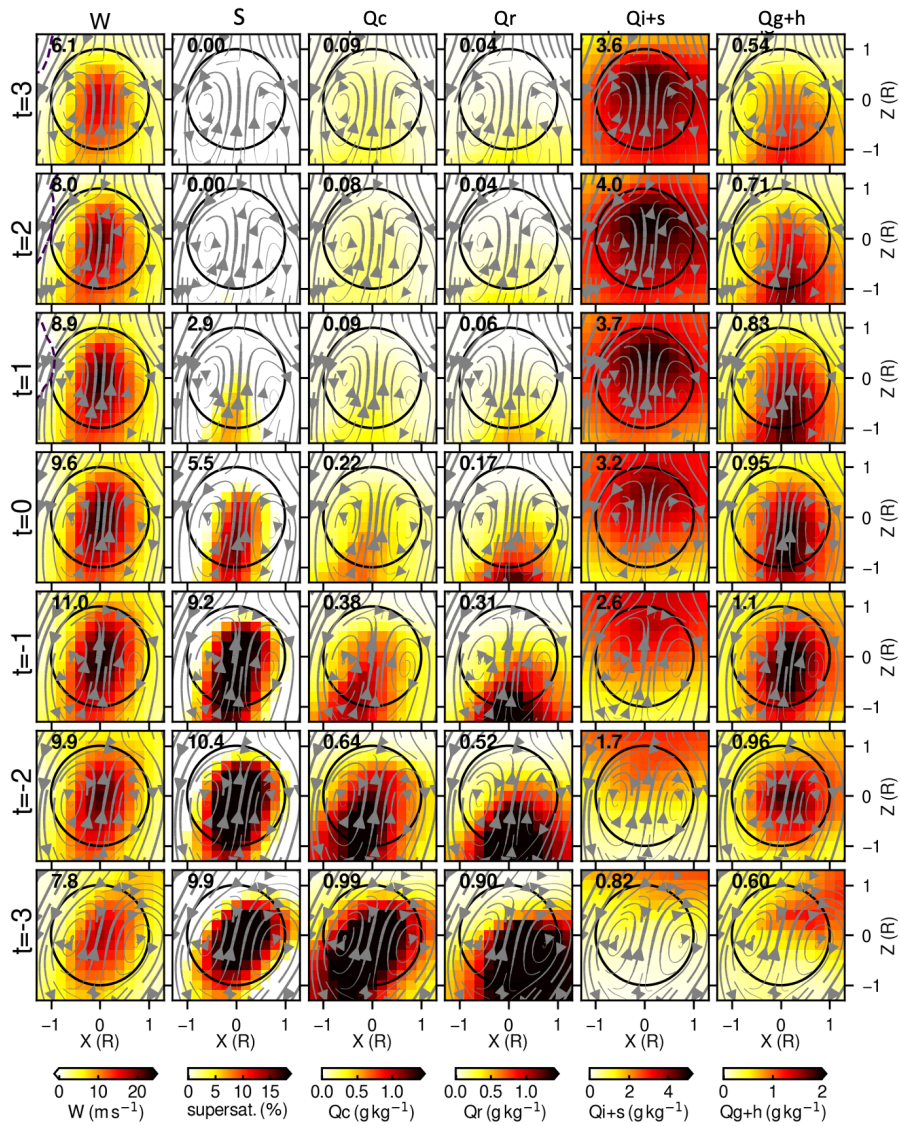
1356

Figure 10. Time series of cross sections along the x-z plane of thermal mean values of vertical velocity, supersaturation values, cloud droplet mass concentration (Qc), rain mass concentration (Qr), (e) ice and snow mass concentration (Qi+s), and graupel and hail mass concentration (Qg+h), for composites of all tracked thermals scaled by their radius. The time unit is minute.

1360
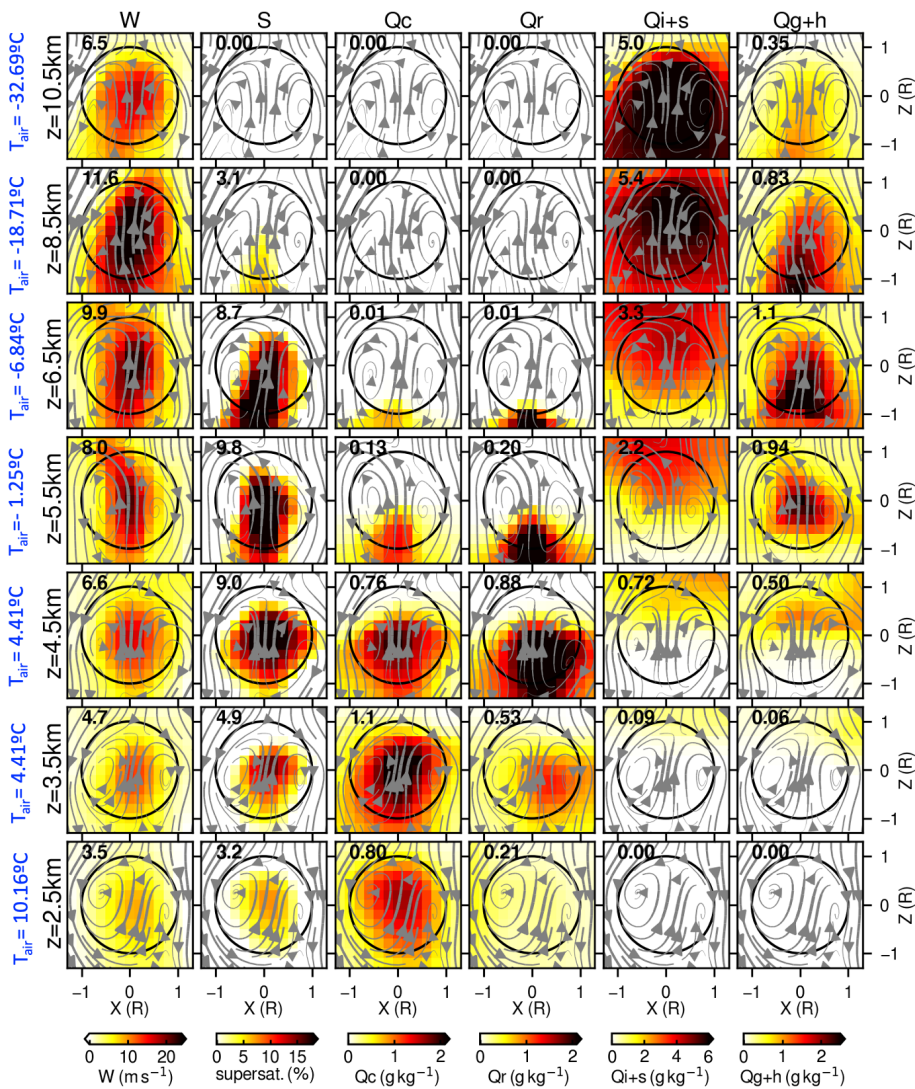
Figure 11. Similar to Fig. 10, but composited at different altitude levels. Note that the shade scales are different from Fig. 10 for clarity.
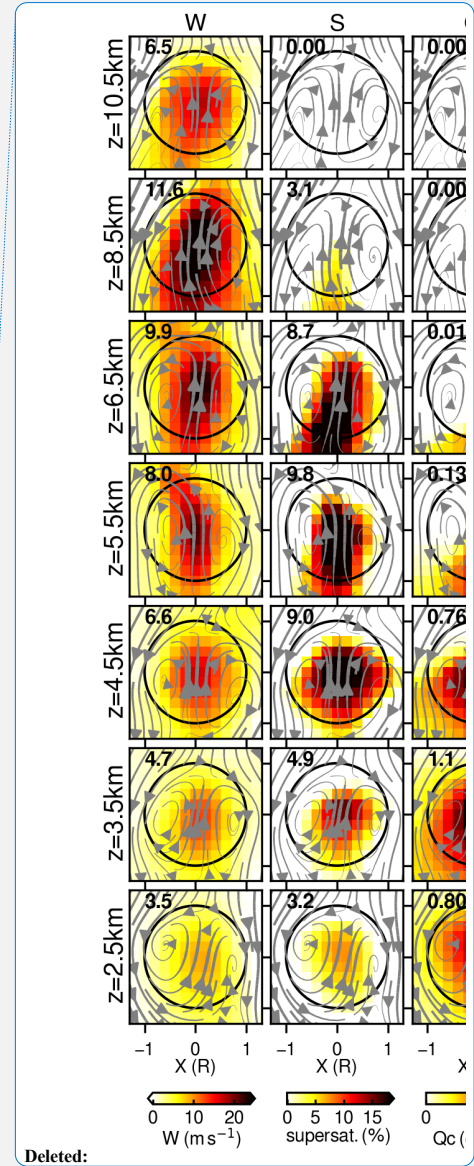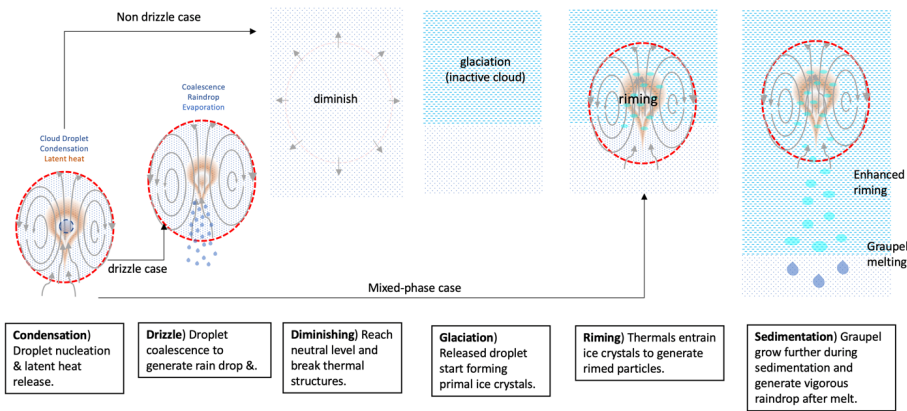
1366

1367   a)
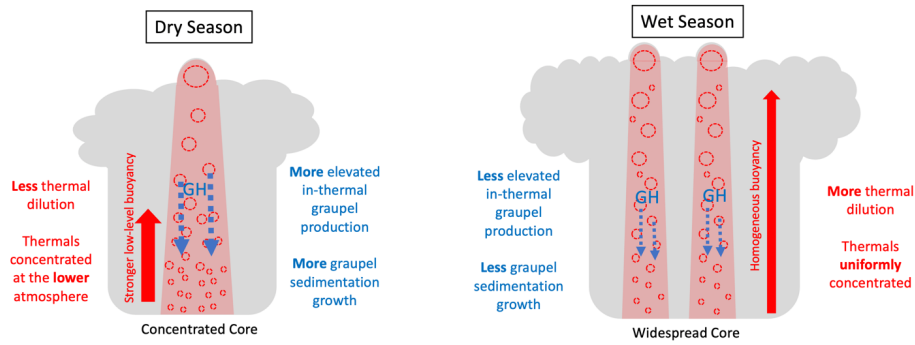
1368

1369   b)

1370   Figure 12. (a) Diagram of the suggested mechanisms for generating graupel and hail through
1371   thermal processes. (b) Diagram of thermal characteristics in deep convection in the dry and wet
1372   seasons.

1373